International Journal of Biological Macromolecules 381 (2026) 153953

Contents lists available at ScienceDirect

International Journal of Biological Macromolecules

journal homepage: www.elsevier.com/locate/ijbiomac

Injectable carrageenan-based hydrogel with piezoelectric particles for potential regenerative applications

Arianna Rossi [a], Noemi Ravaglia [a,b], Federica Arienti [a,c], Pietro Galizia [a], Massimiliano Labardi [d], Carlo Baldisserri [a], Rosa Mancinelli [b], Sabrina Angelini [c,f], Monica Montesi [a], Alessio Bucciarelli [e], Elisa Mercadelli [a], Silvia Panseri [a,*]

[a] Institute of Science, Technology and Sustainability for Ceramics, National Research Council of Italy (CNR-ISSMC), Via Granarolo 64, 48018, Faenza, Italy
[b] Department of Neuroscience, Imaging and Clinical Science, University of Studies "G. D'Annunzio", 66100, Chieti, Italy
[c] Department of Pharmacy and Bio Technology-FaBiT, Alma Mater Studiorum University of Bologna, Via Irnerio 48, 40126 Bologna, Italy
[d] Institute for Chemical-Physical Processes, National Research Council of Italy (CNR-IPCF), Largo Pontecorvo 3, 56127, Pisa, Italy
[e] BIOtech Research Center, Department of Industrial Engineering, University of Trento, Via delle Regole 101, Mattarello, 38123, Trento, Italy
[f] Clinical Pharmacology Unit, IRCCS Azienda Ospedaliero-Universitaria di Bologna, Via G. Massarenti 9, 40138 Bologna, Italy

ARTICLE INFO

Keywords:
Collagen
Hyaluronic acid
Barium titanate
Ultrasound
Extracellular matrix mimicry
Soft tissue regeneration
Minimally invasive therapy

ABSTRACT

Injectable hydrogels represent a promising strategy for minimally invasive regenerative medicine, enabling the delivery of biomimetic microenvironments directly to irregular tissue defects. Here, we present a multi-responsive, ECM-like injectable hydrogel based on κ/λ-carrageenan, hyaluronic acid, and type I collagen, designed to combine ion-triggered gelation with ultrasound-activated piezoelectric functionality. Gelation occurs rapidly upon exposure to physiological ions, allowing straightforward injection through fine-gauge needles without the need for external crosslinkers or harsh conditions. The incorporation of submicrometric barium titanate particles confers piezoelectric responsiveness, enabling the conversion of ultrasound-induced mechanical stimuli into localised electrical cues. The resulting hydrogels exhibit mechanical properties (Young's modulus 4–9 kPa) and viscoelastic behaviour comparable to native soft tissues, alongside a highly interconnected porous architecture suitable for mass transport and cell infiltration.

In vitro studies demonstrate cytocompatibility with fibroblasts, myoblasts, neuronal-like cells, and macrophages, supporting cell viability and proliferation while promoting a pro-regenerative macrophage phenotype. Preliminary ultrasound stimulation experiments confirm that piezoelectric activation does not impair cell viability, establishing a safe basis for future functional investigations.

Overall, this work introduces a user-friendly, cost-effective, and multifunctional injectable hydrogel platform with potential for minimally invasive and remotely activated regenerative therapies.

1. Introduction

Trauma is the third leading cause of death worldwide, and even when not fatal, severe injuries often impair tissue function. Likewise, many diseases cause cellular and microenvironmental damage that compromises tissue functionality. In several clinically relevant conditions, such damage progresses toward large-scale tissue loss that exceeds the intrinsic regenerative capacity of the body. Typical examples include full-thickness skin loss following burns or trauma, myocardial infarction associated with massive cardiomyocyte death, and critical-size bone defects resulting from fractures, tumor resection, or infection. These conditions frequently lead to permanent functional impairment because spontaneous regeneration is limited and fibrotic tissue replaces native structures, highlighting a major unmet clinical need for advanced regenerative strategies [1–7].

Regenerative medicine, therefore, faces major challenges. In particular, restoring tissue architecture and function in large-volume defects requires biomaterial systems capable not only of supporting cell survival but also recreating a permissive microenvironment for regeneration. Developing innovative, patient-tailored strategies that are user-friendly and cost-effective requires an interdisciplinary approach, integrating expertise from chemistry, physics, engineering, and biology.

* Corresponding author.
E-mail address: silvia.panseri@cnr.it (S. Panseri).

https://doi.org/10.1016/j.ijbiomac.2026.153953
Received 10 March 2026; Received in revised form 31 July 2026; Accepted 5 August 2026
Available online 7 August 2026

Biomaterial-based approaches have emerged as promising tools to address these challenges [8]. In particular, in the context of extensive cell and extracellular matrix (ECM) loss, as observed in critical-size defects that cannot spontaneously heal without surgical intervention, the design of tailored three-dimensional biomaterials becomes essential. These biomaterials (*i.e.* scaffolds) should be capable of supporting cell growth by replicating the physical, chemical, and mechanical features of native ECM [9]. Several scaffold fabrication techniques, including electrospinning [10,11], 3D bioprinting [12,13], and freeze casting [14,15], have been developed to regenerate tissue structures. However, these scaffolds are typically pre-formed in the laboratory, making it difficult to precisely match their size and shape to variable defects. Moreover, their implantation often requires highly invasive surgery, particularly for complex tissues such as the brain, spinal cord, joints, and muscles [16,17]. These limitations restrict their clinical applicability in routine treatments.

Injectable hydrogels represent a promising alternative among emerging biomaterials. Their minimally invasive administration eliminates the need for open surgery, as they can be directly delivered *in vivo* through needles or catheters. This approach offers several advantages for both patients and clinicians, including reduced pain, faster recovery, lower costs, and fewer complications [18]. Importantly, their injectability makes them particularly suitable for treating irregular and deep tissue defects such as post-infarct myocardial regions, volumetric muscle loss, and complex bone lesions, where precise defect filling is essential but difficult to achieve with pre-formed scaffolds [19]. In detail, injectable hydrogels are three-dimensional networks of natural or synthetic polymers with a highly hydrated structure that mimics the ECM, creating a favourable microenvironment for cells and bioactive molecules. Their soft texture contributes to reducing local inflammatory responses after injection, further enhancing biocompatibility in both *in vitro* and *in vivo* settings [20]. While mimicking ECM architecture is essential, stimulating tissue regeneration through additional cues is equally important. For example, in nervous and muscle tissues, bioelectricity plays a fundamental role in both normal function and repair. Stimuli that intrinsically activate or modulate the bioelectricity can significantly enhance regenerative processes, such as those involved in wound healing [21]. Traditional electrical stimulation systems often rely on direct coupling, in which conductive electrodes make physical contact with the target tissue or scaffold [22]. Although widely adopted, this method requires external wiring, which poses clinical challenges, especially in deep or complex lesions, due to risks of infection, discomfort, and limited patient mobility. Wireless approaches, such as capacitive and inductive coupling, have been explored to overcome these limitations, but direct coupling remains the predominant method in both clinical and research contexts.

Here, we propose an injectable, multi-stimuli-responsive hydrogel for tissue regeneration. The hydrogel undergoes sol–gel transition in response to ions, and the incorporation of piezoelectric particles enables responsiveness to external stimuli (*e.g.*, ultrasound).

Among potential polymers, κ/λ-carrageenan was selected as the hydrogel backbone. Extensively used in the literature as a macromolecular crowding (MMC) agent, carrageenan mimics the crowded *in vivo* environment and can enhance cell proliferation or differentiation depending on conditions [23,24]. It is a water-soluble, linear sulfated polysaccharide with excellent ion-responsive gelation properties [25], widely employed in the food and cosmetics industries and already approved by European Food Safety Authority (EFSA) [26] and U.S. Food and Drug Administration (FDA) [27]. Derived from red seaweed, carrageenan also represents a sustainable raw material. To improve the biofunctionality of our system, we incorporated key ECM components, including hyaluronic acid (HA) and type I collagen, into the formulation [28,29]. Notably, HA plays a crucial role in ECM remodelling and has been linked to scar-free muscle tissue regeneration [30–32]. Furthermore, piezoelectric barium titanate (BTO) particles [33,34] were embedded to confer multi-stimuli responsiveness, thanks to their excellent piezoelectric properties. Ultrasound-induced mechanical deformation of these particles generates local electric currents, thereby enhancing tissue regeneration [35].

Our comprehensive study demonstrates that the resulting hydrogel is straightforward to formulate, user-friendly, and cost-effective. Its injectability and responsiveness to external stimuli make it particularly suitable for minimally invasive surgery and open new perspectives for at-home post-surgical treatments through simple ultrasound applications.

2. Materials and methods

2.1. Materials

k/λ-Carrageenan (Carr, Sigma Aldrich), hyaluronic acid (HA, molecular weight: 1700 kDa, DSM), collagen from bovine tendon (Coll, Sigma Aldrich), barium titanate (IV) particles (BTO, Sigma Aldrich), acetic acid (Sigma Aldrich), potassium chloride (KCl, Sigma Aldrich), sodium hydroxide (NaOH, Sigma Aldrich), urea (Sigma Aldrich), running buffer 10X (Bio-Rad), Laemmli Sample Buffer (Bio-Rad), Mini-PROTEAN TGX Precast Gels 5–20% (Bio-Rad), Coomassie Brilliant Blue G-250 (Bio-Rad), methanol (Sigma Aldrich), DC Protein Assay Kit (Bio-Rad), paraformaldehyde (PFA, Sigma Aldrich), phosphate-buffered saline (1X) w/o Ca and Mg (PBS, Gibco), αMEM (Gibco), EMEM (ATCC), DMEM/F12 no phenol red (Gibco), DMEM high glucose (Gibco), foetal bovine serum (FBS, Gibco), penicillin/streptomycin mixture (pen/strep, Gibco), trypsin 0.5% EDTA (Gibco), trypan blue (Sigma Aldrich), MTT reagent (Sigma Aldrich), dimethyl sulfoxide (DMSO, Sigma Aldrich), LIVE/DEAD Viability/Cytotoxicity Kit (Invitrogen), triton X − 100 (Sigma Aldrich), ActinRed 555 ReadyProbes reagent (Invitrogen), 4′,6-diamidino-2-phenylindole dihydrochloride (DAPI, Invitrogen) reagent, tri reagent (Invitrogen), Directzol RNA MiniPrep kit (Zymo Research), TaqMan Gene Expression Assays (Applied Biosystems), and polydimethylsiloxane (PDMS, Sylgard® 184, Merck) were purchased and used without any further purification.

2.2. Collagen solubilisation and characterisation

Collagen from bovine tendon was solubilised following the protocol described by Pei Y. *et al.* Briefly, 1 g of collagen was immersed in 100 g of a NaOH/urea/H_2O solution (7:12:81 g) and frozen for 3 h at −80 °C, thawed for 1 h at room temperature, frozen again for 3 h at −80 °C, and finally thawed overnight at 4 °C. The solid phase was separated using a sieve and dissolved in 0.02% (w/v) acetic acid. Collagen quality was assessed by SDS-PAGE. The sample was diluted to a final concentration of 0.5 mg/mL in 1× Laemmli Sample Buffer and Milli-Q water, heated at 95 °C for 5 min, and 30 μL were loaded into each well of a Mini-PROTEAN TGX Precast Gel (5–20%). Electrophoresis was performed in 1X Running Buffer at 200 V for 1 h. The gel was rinsed in Milli-Q water, stained with Coomassie Brilliant Blue (0.0025 g/mL in methanol/acetic acid/water, 50:20:30 mL) for 30 min under agitation, and destained with methanol/acetic acid/water (20:10:70 mL). Imaging was carried out using a Gel Doc XR+ Gel Documentation System (Bio-Rad).

Collagen quantification was performed using the DC Protein Assay Kit according to the manufacturer's instructions ($n = 3$).

2.3. Hydrogel formulation

All hydrogel components were prepared separately. Carrageenan (Carr), described by the manufacturer as predominantly κ-carrageenan with lesser amounts of λ-carrageenan, was dissolved at 1.5% (w/v) in Milli-Q water at 70 °C under magnetic stirring using a hot plate stirrer equipped with a temperature probe for continuous temperature monitoring. Hyaluronic acid (HA) was dissolved at 3% (w/v) in Milli-Q water under stirring for 2 h. Collagen (Coll) was solubilised as described above and the pH was adjusted to 7.4 using 5 M acetic acid.

Carr, HA, and Coll were mixed to achieve final concentrations of 0.75% (v/v), 0.3% (v/v), and 0.0375% (v/v), respectively (Carr_HA_Coll). Three control formulations were prepared: Carr (0.75% v/v), Carr_HA (0.75% v/v Carr and 0.3% v/v HA), and Carr_Coll (0.75% v/v Carr and 0.0375% v/v Coll).

To obtain a multi-stimuli-responsive hydrosol, BTO particles ($BaTiO_3$, 99% purity; average particle size ≈ 700 nm), exhibiting a tetragonal phase and submicrometric particle size (Fig. SI 1,2), were added to Carr_HA_Coll. BTO particles were poled at room temperature using a custom-built corona discharge setup. Two different sets of parameters were employed for corona poling. In the first method, a voltage of 20 kV was applied for 5 min at room temperature, with the electrode positioned 5 cm from the sample surface, while in the second method, a voltage of 7 kV was applied for 5 min at 100 °C, with the electrode positioned 1 cm from the sample surface, and then cooled down to 35 °C. The effectiveness of the poling methods on BTO powder was then characterised by piezoresponse force microscopy (PFM). BTO nanoparticles were deposited by drop casting of a diluted dispersion (0.5 mg/mL) in acetone on both doped silicon substrates and gold-coated doped silicon, in order to check the effect of the substrate on the poling efficiency.

BTO was resuspended at 25 mg/mL in Milli-Q water and sonicated for 5 min (20 kHz, 130 W, 20% amplitude). Carr_HA_Coll was supplemented with BTO at final concentrations of 0.5–8 mg/mL. Gelation was induced by 5% KCl (v/v) in cell culture medium. Hydrosols were either extruded through a 30G needle into a 5% KCl (v/v) in cell culture media solution to form spheres (Video SI 1 and Fig. 1A), cast into custom 3D-printed moulds (Fig. 1B), or poured into well plates (96-, 24-, or 6-well) depending on the downstream analysis. For casted samples, 5% KCl was applied to the substrate, the mixture was poured, and an additional layer of KCl solution was sprayed on top. Samples were incubated for 10 min at 37 °C, then submerged in 5% KCl for another 10 min before being transferred to fresh medium.

2.4. Fourier transform infrared (FTIR) spectroscopy analysis

Infrared spectroscopy experiments were carried out on raw materials (carrageenan, hyaluronic acid, collagen, and BTO) in powder form and hydrogels, both prior and after freeze drying, (Carr, Carr_HA, Carr_Coll, Carr_HA_Coll, Carr_HA_Coll_BTO with BTO at 0.5 mg/mL) using a Nicolet™ iS™ 5 FTIR spectrometer (Thermo Fischer instrument) equipped with an internal reflection element (ATR crystal) *i.e.*, a diamond crystal. Collected spectra, obtained by means of 16 scans in the 490–4000 cm^{-1} range, have a resolution of 4 cm^{-1}.

2.5. Dynamic mechanical analysis (DMA)

DMA was performed on Carr, Carr_HA, Carr_Coll, Carr_HA_Coll, and Carr_HA_Coll_BTO hydrogels (BTO at 0.5, 3, and 8 mg/mL) to determine Young's modulus using a DMA Q800 (TA Instruments). Hydrogels were cast as discs (35 mm diameter, 3 mm thickness), incubated overnight in cell culture medium at 37 °C, and punched into 8 mm × 3 mm specimens. Compression testing was carried out in submerged conditions at 37 °C, and Young's modulus was calculated from the linear region of the stress–strain curve (0–10%) ($n = 5$).

2.6. Rheology

Rheological analyses were performed using a Bohlin C-VOR 120 rotational rheometer equipped with a thermostatic unit (KTB 30). Hydrogel discs (35 mm diameter, 3 mm thickness) were incubated overnight in cell culture media at 37 °C. A serrated stainless-steel parallel-plate geometry (40.0 mm diameter; 2.3 mm gap) was used. Small-amplitude oscillatory shear (SAOS) tests were performed at 37 °C. The linear viscoelastic region (LVER) was identified by a stress sweep (0.1–5000 Pa) at 1 Hz, followed by a frequency sweep (0.01–10 Hz) at 5 Pa ($n = 5$). Carr, Carr_HA, Carr_Coll, Carr_HA_Coll, Carr_HA_Coll_BTO (BTO at 0.5 mg/mL) were characterised following previously published procedures [36].

2.7. Scanning electron microscopy

Hydrogel porosity was assessed by SEM. Hydrogels (6.4 mm diameter, 3 mm thickness) were frozen in liquid nitrogen and freeze-dried for 48 h (−40 °C to +25 °C; 0.086 mbar). Scaffolds were cut in half, mounted on aluminium stubs with carbon tape, and gold-sputtered using a Polaron Sputter Coater E5100. Imaging was performed using a Stereoscan 360 SEM (Cambridge Instruments) ($n = 3$ replicates, at least 5 images per condition per replicate).

The SEM segmentation was done using a superpixel segmentation algorithm (jSLIC) in Fiji (v.1.54p). This algorithm allows to separate the initial image (Fig. SI 3A) in superpixel (Fig. SI 3B) using two parameters:

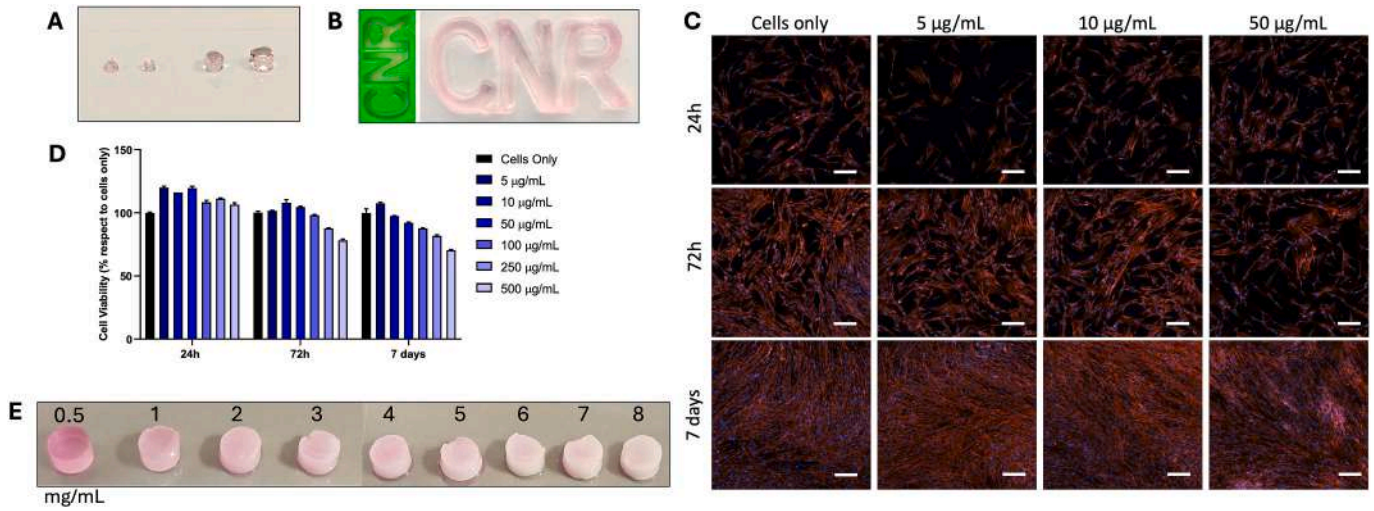

Fig. 1. A: Carr_HA_Coll hydrosol injected through a 30G needle. B: Hydrosol cast in custom 3D-printed mould. C-D: Preliminary cytotoxicity evaluation of BTO on WS1 cells cultured in 2D standard conditions. C: Morphological evaluation on WS1 cells after 24 h, 72 h and 7 days of culture with different concentrations of BTO particles. Actin filaments in red; cell nuclei in blue. Scale bars: 200 µm. D: Cell proliferation measured by PrestoBlue test after 24 h, 72 h and 7 days of culture (mean ± SEM, $n = 3$). α = ****p value ≤0.0001 *vs* all the other concentrations. E: Carr_HA_Coll with different concentrations of BTO (0.5–8 mg/mL), minor shape irregularities are attributable to demolding from the 96-well plate using a spatula.

the Initial grind size and the regularisation which has been selected manually for each image to capture the pores. Then each superpixel was saved as a ROI and thus can be selected (Fig. SI 3C) and used to compose a mask highlighting the pores (Fig. SI 3D). The masks were then analyzed to determine the area, the equivalent diameter (i.e., the diameter corresponding to a perfectly circular pore), the aspect ratio, and the symmetry.

2.8. Piezoresponse force microscopy (PFM)

Converse piezoelectric coefficient d_{33} of single BTO particles was measured by Piezoresponse Force Microscopy (PFM), a local probe technique based on Atomic Force Microscopy (AFM). A recently introduced non-contact piezoresponse technique [37] has been used that allows measurement of particles adhering to a flat, conducting substrate avoiding dragging of the sample during scanning, that is hardly achievable with conventional contact-mode PFM. The AFM used was a NanoScope IIIa with MultiMode head, equipped with gas cell and ADC5 extension (Veeco Instruments Inc., USA). Non-contact type AFM cantilevers (Nanosensors PPP-NCLPt, platinum-iridium coated silicon tips, spring constant ~40 N/m, resonant frequency $f_0 \sim 156$ kHz, quality factor $Q_0 \sim 500$ in air, tip radius ~ 30 nm) were operated in constant-excitation frequency modulation (CE-FM)-AFM mode, with a free oscillation amplitude of $A_0 \sim 20$ nm. Distance stabilisation is obtained by feedback on the oscillation amplitude. An oscillating voltage $V(t) = V_{dc} + V_{ac}\cos(2\pi ft)$ is applied to the probe as customary in PFM, with the sample conductive substrate grounded. The typical frequency used was around $f \sim 80$ Hz. The oscillation amplitude signal $A_f(t)$ from the FM-AFM controller (PLLProII, RHK Technology, Troy, USA) is demodulated at frequency f by a dual lock-in amplifier (SRS830DSP, Stanford Research Systems, USA) whose output (ΔA) was acquired through the auxiliary acquisition channels of our AFM. The latter output represents the measurement of the surface displacement induced by the applied electric field, and therefore of the converse piezoelectric effect. By dividing such surface displacement by the applied voltage V_{ac}, the piezoelectric coefficient d_{33} is obtained. Noteworthy, the PFM method usually yields underestimated values of piezoresponse on stiff materials like BTO ceramics. This is because the local electric field produced by the sharp AFM probe tip is strongly concentrated on a small sample area of a few hundreds of nm^2, therefore the surrounding material is concerned by much lower electric field and its piezoelectric deformation is much reduced compared to the center region. If the material is very stiff, as in the case of ceramics, internal elasticity of the material contrasts strongly the local deformation of the surface area faced to the tip, giving raise to the so-called clamping effect, limiting the actual local deformation by piezoelectric effect.

2.9. Stability evaluation

Hydrogel discs (22 mm diameter, 3 mm thickness) were incubated in cell culture medium at 37 °C for up to 42 days under two conditions: (i) partial medium replacement (removal of 500 μL and addition of 750 μL), and (ii) medium supplementation only (250 μL added every 2–3 days). Samples were weighed at days 0, 7, 14, 21, 28, 35, and 42. Data are expressed as percentage of the initial mass ($n = 4$).

2.10. In vitro biological evaluation

The human fibroblast cell line WS1 (ATCC CRL-1502), neuroblastoma cell line SH-SY5Y (ATCC CRL-2266), murine myoblast cell line C2C12 (ATCC CRL-1772), and murine macrophage cell line RAW 264.7 (ATCC TIB-71) were used. Cells were cultured under standard conditions (37 °C, 5% CO_2, controlled humidity) in their respective media (WS1: αMEM; SH-SY5Y: 1:1 mix of EMEM and DMEM/F12 no phenol red; RAW 264.7 and C2C12: DMEM high glucose) supplemented with 10% FBS and 1% pen/strep. Cells were detached by trypsinisation, centrifuged, counted by Trypan Blue exclusion, and handled under sterile conditions.

For the initial BTO particles' cytocompatibility screening under standard 2D conditions, WS1 cells were seeded at 2×10^3 cells/well in 96-well plates. After 24 h, the cell culture medium was replaced with BTO suspensions (5, 10, 50, 100, 250 and 500 μg/mL). Brightfield images were acquired at 24 h using an inverted Ti-E fluorescence microscope (Nikon).

For the biological evaluation of the hydrogels, cells were encapsulated into different hydrogel formulations at the following densities: WS1 (7.5×10^5/mL), SH-SY5Y (5×10^6/mL), C2C12 (6×10^6/mL), RAW 264.7 (2×10^6/mL). Hydrosols were then cast in 96-well plates as described above.

2.11. Viability and proliferation analysis

Quantitative cell viability and proliferation over time were performed both on standard 2D cell culture for the initial screening of BTO particles, and on cells encapsulated into several hydrogels at different time-points (WS1, C2C12 and SH-SY5Y: d1 and d3; RAW 264.7: day 2) and formulations using the PrestoBlue assay according to the manufacturer's instructions. The reagent was added to the culture medium at 10% v/v, and incubated for 2 h at 37 °C in a humidified 5% CO_2 atmosphere. The reagent is converted by living cells in fluorescent resorufin, which was detected by using the Fluoroskan Microplate Fluorometer (Thermo Fisher Scientific), setting the excitation wavelength equal to 544 nm, whereas the emission wavelength to 590 nm. A hydrogel without cells was used as blank and its background value was then removed from all the viability data. ($n = 3$ biological replicates, each measured in technical triplicate).

A qualitative analysis to evaluate the cell viability encapsulated into the hydrogels was performed at different time points (WS1, C2C12 and SH-SY5Y: day1 and day3; RAW 264.7: day 2) using LIVE/DEAD® assay following the manufacturer's instructions. Briefly, cells were washed with PBS 1× and incubated with 1.3 μM of Calcein AM and 4 μM of Ethidium homodimer-1 for 15 min at 37 °C and 5% CO_2. Images of live cells stained in green and dead cells in red were acquired by using an inverted Ti-E fluorescent microscope (Nikon). Two samples for each group were analysed ($n = 2$ biological replicates, at least 3 images per condition per replicate).

2.12. Cell morphology evaluation

For morphology analysis of WS1 cells exposed to 5, 10 and 50 μg/mL BTO, cells were fixed in 4% PFA after 1, 3 and 7 days, permeabilised with 0.1% Triton X-100, and F-actin filaments were stained using Actin Red 555 ReadyProbes™ Reagent, followed by nuclear counterstaining with DAPI (600 nM). Images were acquired using an inverted Ti-E fluorescent microscope (Nikon) ($n = 2$ biological replicates, at least 3 images per condition per replicate).

2.13. Gene expression analysis

To assess the polarisation of RAW 264.7 cells embedded for 48 h in the hydrogels, RNA was extracted from hydrogels using TRI Reagent followed by purification with the Direct-zol RNA MiniPrep Kit. RAW 264.7 cells seeded at 2×10^5 cells/well in 6 well-plate were used as control group.

RNA purity and concentration were measured using NanoDrop One Microvolume UV–Vis Spectrophotometer (Thermo Scientific). cDNA was synthesised from 500 ng RNA using the High-Capacity cDNA Reverse Transcription Kit. Gene expression of TNF-α (Mm00443258_m1), IL-10 (Mm01288386_m1), and GAPDH (Mm99999915_g1) was quantified using TaqMan assays on a QuantStudio 1 Real-Time PCR System (Applied Biosystems). The relative quantification of target gene was assessed with the Comparative Threshold (Ct) method (ΔΔCt) [38] ($n = 2$ biological replicates, each

measured in technical triplicate).

2.14. Ultrasound application set up

Ultrasound (US) stimulations were performed using a Vibra-Cell VCX 130 ultrasonic processor (Sonics & Materials Inc.) equipped with a 6 mm diameter probe, operating at 20% amplitude and a frequency of 20 kHz. To optimise US stimulation, a custom culture chamber was designed and manufactured by a mould-casting process of PDMS. Based on calculations derived from available data [39], a 2-cm-thick layer of 10:1 cross-linked PDMS (thickness of the PDMS cap) is expected to reduce ultrasound power transmission by approximately two orders of magnitude, in order to obtain the final stimulation intensity used of 900 mW/cm^2. PDMS was selected for its favourable mechanical and acoustic properties, including an acoustic impedance comparable to that of cell culture media, making it suitable for effective ultrasonic transmission [39,40]. The experimental setup allowed for consistent and reproducible ultrasound exposure. An acoustic intensity of 900 mW/cm^2 was applied. Both Carr_HA_Coll_BTO and Carr_HA_Coll hydrogels, with embedded WS1 cells, were placed in the chamber, immersed in culture medium, and subjected to a 60-second ultrasound stimulation once daily for five consecutive days. The cell viability was qualitatively and quantitatively assessed through LIVE/DEAD assay (day 3 and day 5, $n = 3$) as described above and MTT assay (day 1, day 3 and day 5) following the manufacturer's instructions. Briefly, MTT reagent [3-(4,5-dimethylthiazol-2-yl)-2,5-diphenyltetrazolium bromide] (5 mg/mL) was prepared in PBS 1X, added to the culture medium at 10% v/v, and incubated for 2 h at 37 °C in a humidified 5% CO_2 atmosphere. The medium was then removed, and the resulting formazan crystals generated by metabolically active cells were dissolved in DMSO. For the hydrogels, the samples were crushed to release formazan crystals and centrifuged (3 min, 15,000 rpm). Blank hydrogels without cells were used for background subtraction. Absorbance values, measured at 570 nm using a Multiskan FC microplate photometer (Thermo Scientific), were proportional to the number of viable cells ($n = 9$ biological replicates, each measured in technical triplicate).

2.15. Statistical analysis

The results were plotted as average ± standard deviation. 2D WS1 viability, 3D WS1 ultrasound experiment viability and RAW 264.7 gene expression data were analysed by Two-way analysis of variance (Two-way ANOVA), followed by Tukey's Multiple Comparisons test. Young's Moduli data were analysed by One-way analysis of variance (One-way ANOVA), followed by Tukey's Multiple Comparisons test. All the statistical analyses were performed by GraphPad Prism Software (Version 8.0). All data were included in the analyses, and no outliers were excluded or removed during correlation analyses, as no exclusion criteria or outlier filtering procedures were applied. Statistically significant differences for the stability data are reported in the graph, *p value ≤0.05, **p value ≤0.01, ***p value ≤0.001 and ****p value ≤0.0001.

All computations for data image segmentation were performed in Python 3.11.8 (Linux) using open-source scientific libraries. Data handling and I/O were done with pandas 1.5.3 and NumPy 1.24.0; correlation coefficients and hypothesis tests used SciPy 1.14.1 (Spearman's ρ), and visualisations (triangular heatmaps and scatter plots) were produced with Matplotlib 3.6.3. We analysed the variables using non-parametric rank-based correlation to accommodate skewed distributions and potential outliers. Specifically, pairwise Spearman's ρ coefficients were computed for all numeric variable pairs using pairwise complete observations. Variables with fewer than three overlapping observations per pair were omitted for that pair; fully constant variables were excluded from correlation estimates. Two-sided p-values were obtained from the Spearman test; statistical evidence was interpreted at $\alpha = 0.10$, and for reporting/visualisation $p < 0.001$ was displayed as 0. Effect sizes are presented as Spearman's ρ with corresponding p-values. Results are visualised as triangular matrices where the lower triangle shows a heatmap of ρ (range −1 to +1) and the upper triangle reports the numeric values (ρ for the correlation figure; p for the significance figure), preserving the original variable labels and symbols. To aid interpretation of relationships deemed noteworthy ($p < 0.10$), we generated bivariate scatter plots using pairwise-complete data and annotated them with ρ and p. All analyses were performed in Python (SciPy/NumPy, Matplotlib), and tables/figures were produced with consistent axis labelling and scaling to ensure legibility. Unless otherwise stated, no multiple-comparison adjustment was applied, and findings should be interpreted as exploratory.

3. Results and discussion

3.1. Hydrogel formulation, characterisation and BTO initial screening

Carrageenan (Carr) is a seaweed-derived polysaccharide widely used in the food and cosmetics industries and is already approved by both the European Food Safety Authority (EFSA) [26] and the U.S. Food and Drug Administration (FDA) [27].

Carr's gelling behaviour depends on temperature and the presence of ions in solution (*e.g.*, KCl), leading to the formation of a stable thermoreversible gel [25]. The Carr used in this study corresponds to a commercially available material described as predominantly κ-carrageenan with lesser amounts of λ-carrageenan. The presence of κ-carrageenan ensures ion-responsive thermoreversible gel formation, while the λ-carrageenan fraction may contribute additional biofunctional effects. In particular, λ-carrageenan has been reported to support extracellular matrix deposition without negatively affecting cell morphology, viability, metabolic activity, or proliferation, suggesting a potential role as a macromolecular crowding agent that enhances the development of a biomimetic microenvironment in tissue engineering applications [41–43].

To obtain a liquid formulation suitable for injection through a 30G needle, ensuring a minimally invasive application, Carr was dissolved at 1.5% (w/v) and maintained at 41 °C. Carr mimics the crowded *in vivo* environment and can enhance cell proliferation and/or differentiation depending on conditions [23,24]. To better reproduce the human extracellular matrix (ECM) [44,45] and enhance the hydrogel's bioactivity, we used Carr (final concentration equal to 0.74% v/v) as the backbone material supplemented with hyaluronic acid (HA, 0.3% v/v) and collagen (Coll, 0.0375% v/v). Both HA and Coll are major ECM components that play key roles in regulating cell differentiation, migration, angiogenesis, and inflammation [28,29]. The collagen used (bovine tendon) was solubilised following the protocol explained in Collagen Solubilisation material and methods section; its purity was assessed by SDS-PAGE (Fig. SI 4), and its concentration was determined using the DC protein assay (0.68% v/v).

The resulting hydrosol could be easily injected through a 30G needle under manual pressure, without observable clogging or phase separation (Fig. 1A; Video SI1). Injection was reproducible across multiple samples and remained stable immediately before gelation. This behaviour is particularly relevant for minimally invasive delivery, as it indicates adequate flowability at high shear conditions typically associated with fine-gauge needles. This feature provides a significant advantage over other injectable systems, whose delivery through fine needles can be hindered by high material viscosity [46,47]. Gelation occurred within a few minutes (*i.e.* <5 min) upon contact with 5% (v/v) KCl in cell culture medium. The sol–gel transition was visually confirmed by the ability of the gels to be removed from the support in which they were formed while maintaining the geometry of the support (*e.g.*, 96-well plate, 24-well plate (Fig. SI 5). Moreover, unlike certain hydrogels whose gelling agents require specific conditions, such as UV exposure, to initiate gelation, carrageenan offers a more versatile alternative by leveraging physiological potassium ions [48]. This provides a flexible and practical cross-linking strategy, particularly valuable in contexts where limited

light penetration or potential cross-linker toxicity are concerns [49,50]. The hydrosol also exhibited high moldability, as shown in Fig. 1B: it was cast in a custom 3D-printed mould and accurately replicated the mould geometry, indicating sufficient pre-gel viscosity and structural stability to maintain spatial adaptability prior to ionic crosslinking. Since pathological lesions rarely present a defined shape, the ability of the hydrogel to fill irregular defects *via* simple injection represents a significant advantage over scaffolds produced using freeze-casting, 3D bioprinting, or electrospinning [51–53].

Furthermore, BTO particles were incorporated to provide multi-stimuli responsiveness. Ultrasound-induced mechanical deformation of BTO generates local electric currents that can promote tissue regeneration, effectively introducing a controlled bioelectric stimulus through ion movements and endogenous ionic currents within the surrounding microenvironment. BTO particles are widely reported to exhibit high biocompatibility and chemical stability in physiological environments, with low intrinsic cytotoxicity and favourable interactions with several cell types [54]. This behaviour is attributed to their chemical inertness and the absence of harmful ion release. *In vivo* studies further support the safe integration of BTO-containing scaffolds, where enhanced tissue formation has been observed without adverse local effects [55].

Non-contact PFM measurements were performed on nanoparticle clusters, showing that different particles within the same cluster exhibited different apparent piezoelectric coefficients (Fig. 2).

BTO particles poled at room temperature using method 1 showed the most consistent local electromechanical response, with apparent d_{33} values of approximately 5 pm/V (Fig. SI 7). Based on these results, particles treated under these conditions were selected for the biological studies. Further details on the PFM measurements and corona poling comparison are reported in the Supplementary Materials.

As a preliminary step, BTO biocompatibility was evaluated in 2D cultures of human skin fibroblasts (WS1). Increasing BTO concentrations (0.5–500 μg/mL) were added to the cells, and morphology and viability were assessed after 24 h, 72 h, and 7 days (Fig. 1C, D). No signs of cytotoxicity were observed at 24 h. At later time points, the highest concentrations resulted in a modest reduction in viability, likely reflecting the intrinsic limitations of static 2D cultures when exposed to elevated particle loads. This behaviour is consistent with reports across the literature, where reduced viability at high concentrations is commonly attributed to culture-related constraints rather than true particle-induced cytotoxicity, regardless of particle type [56–58] (Fig. SI 6).

We then investigated whether BTO influenced Carr_HA_Coll gelation and moldability. A broad concentration range (0.5–8 mg/mL) was tested, and no qualitative differences were observed in term of moldability, with the gelation time remaining below 5 min (Fig. 1E). These concentrations are higher than those used in 2D cytotoxicity assays, as the constraints of static monolayers do not apply in 3D systems, where particle dispersion within the hydrogel prevents the viability limitations typically observed in 2D cultures. For characterisation, hydrosols were cast into hydrogel discs using 5% (v/v) KCl in cell culture medium. Gelation occurred within minutes (*i.e.* <5 min), and the hydrogels were easily handled.

To confirm the structural identity, chemical integrity, and successful incorporation of each macromolecular precursor and BTO into the final matrix, FTIR spectra were recorded for each individual component in powder form (*i.e.* Carr, HA, Coll, BTO), and the composite hydrogels (Fig. 3). The spectrum of raw HA displays a broad band around 3300–3400 cm^{-1} assigned to OH and NH stretching vibrations, along with characteristic peaks at ~1610 $cm^{-1}$and ~1405 cm^{-1}, corresponding to the asymmetric and symmetric stretching of the carboxylate groups (-COO-), respectively. The intense band at ~1030 cm^{-1} corresponds to C-O-C ether and pyranose ring stretching. The spectrum of Coll exhibits the characteristic protein signature, including the Amide *I* band at ~1640 cm^{-1} (C═O stretching), Amide II at ~1545 cm^{-1} (N—H bending and C—N stretching), and Amide III at ~1240 cm^{-1}. The preservation of these distinct amide peaks confirms the integrity of the triple-helical structure of collagen. In the Carr spectrum, typical ester sulfate group (S═O) stretching vibrations are visible around 1220–1250 cm^{-1}, alongside the glycosidic linkage region at 900–1050 cm^{-1}. The BTO spectrum shows a strong band starting below 700 cm^{-1} with a minimum near 500–600 cm^{-1}, characteristic of Ti—O stretching vibrations in the perovskite crystal lattice. The composite hydrogel spectrum (Carr_HA_Coll_BTO) clearly demonstrates the successful integration of all constituents into a single, cohesive network. Broadening and intensification of the -OH/ -NH stretching region (3300 cm^{-1}) combined with subtle shifts in the Amide I/carboxylate peak positions (~1640 cm^{-1}) indicate strong intermolecular interactions (*e.g.*,

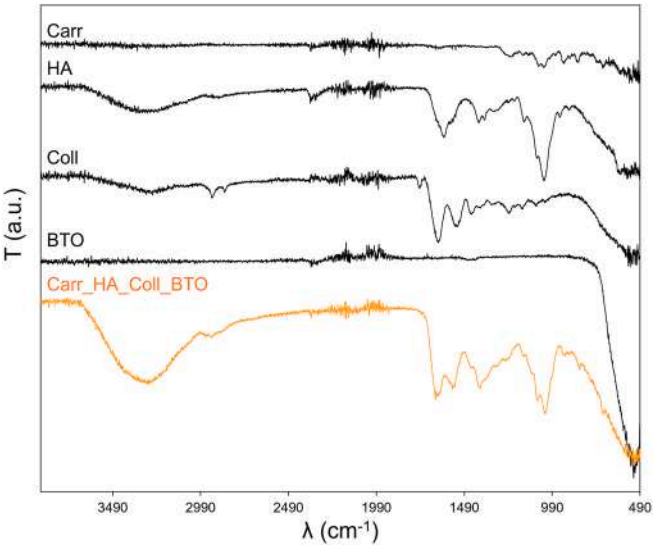

Fig. 3. ATR-FTIR spectra of the starting raw materials, *i.e.* Carr, HA, Coll, BTO and of the resulting Carr_HA_Coll_BTO hydrogel.

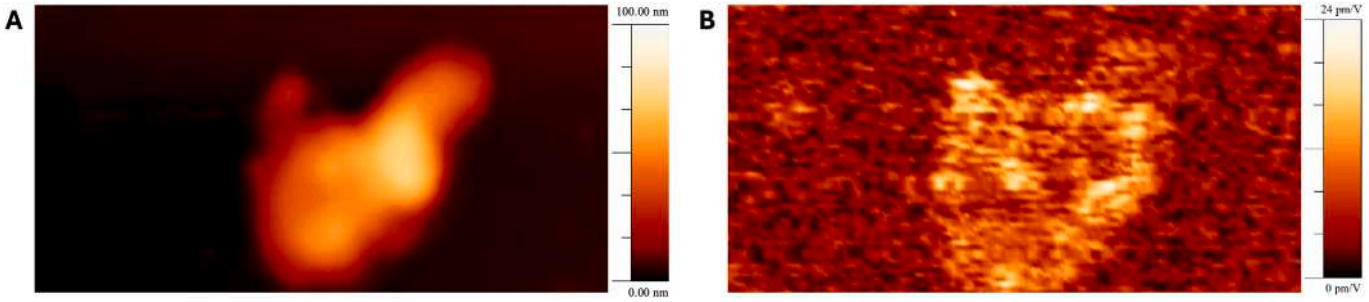

Fig. 2. Topography (A) and piezoresponse (B) images of a typical nanoparticle cluster, cast on a flat conductive (doped silicon) substrate, measured by non-contact piezoresponse force microscopy.

hydrogen bonding and electrostatic interactions) between the polymeric backbones. Furthermore, the simultaneous presence of the polysaccharide fingerprint region (1000–1050 cm^{-1}) and the strong low-wavenumber absorption signature (<700 cm^{-1}) derived from BTO verifies the homogenous entrapment of the inorganic nanoparticles within the macromolecular hydrogel framework. The step-by-step chemical incorporation and structural evolution across all intermediate hydrogel formulations (Carr, Carr_HA, Carr_Coll, Carr_HA_Coll, and Carr_HA_Coll_BTO) were further confirmed by FTIR analysis, as reported in Figs. SI 7 and SI 8.

For soft tissue regeneration, mechanical properties must closely match those of native tissues, as stiffness, together with chemical composition, plays a central role in modulating cell adhesion, spreading, proliferation, and differentiation [50]. Matrix stiffness was assessed *via* dynamic mechanical analysis (DMA). Young's modulus (E) was determined from stress–strain curves in compression under physiological-like conditions (samples submerged in medium at 37 °C). The slope of the linear region between 0 and 10% strain was used to calculate E.

Among the different concentrations tested, three were selected for further experiments (0.5, 3, and 8 mg/mL), representing low, intermediate, and high BTO levels within the investigated range. No statistically significant differences were observed, indicating that BTO does not affect the hydrogel's Young's modulus (Fig. 4A, B). For subsequent studies, the lowest concentration (0.5 mg/mL) was selected for the initial screening, as it allowed us to evaluate the material performance while minimizing the particle load and potential interference with biological responses. From here on, "Carr_HA_Coll_BTO" refers to this concentration. Young's modulus values ranged from 4.4 to 8.7 kPa (Fig. 4A, B), comparable to human soft tissues [59,60]. The lowest value corresponded to Carr alone, while the highest corresponded to Carr_HA_Coll, indicating that the addition of HA and Coll slightly increased stiffness. No statistical difference was found between Carr_HA_Coll and Carr_HA_Coll_BTO, confirming that BTO does not alter mechanical properties.

Rheological analyses further characterised the mechanical behaviour. Oscillatory shear tests were used to determine viscoelastic properties. The linear viscoelastic region (LVER) and critical strain were identified through a stress sweep (Fig. 4C). Critical strain values ranged from 0.60 to 1.48%, indicating the strain threshold at which the hydrogel network begins to deviate from linear viscoelastic behaviour (Fig. 4E). Frequency sweeps performed within the LVER showed that G′ consistently exceeded G″ by one order of magnitude, and G′ was nearly frequency-independent, indicative of a strong viscoelastic gel (Fig. 4D). The predominance of the elastic component was also supported by tan δ = G″/G′ < 1 throughout (Fig. 4E). Values of tan δ close to 0.01 may increase sensitivity to instrumental phase resolution and explain minor signal instabilities. The generalized Maxwell model yielded shear modulus (G) values of 1.17–3.94 kPa, indicating robust mechanical performance, with increases upon addition of each component (Fig. 4E). G′0 represents the elastic (storage) modulus of the hydrogel in the linear viscoelastic region, reflecting the initial stiffness and integrity of the polymer network under small deformations.

The G′0 values obtained in the range 0.96–2.25 kPa indicate that all formulations behave as soft, elastic gels, with modest differences attributable to the different compositions. This stiffness range is well-suited for regenerative medicine applications targeting soft tissues, as it mimics the mechanical environment of native soft biological tissues (Fig. 4E). Hydrogel stability over time was evaluated in conditions mimicking cell culture and physiological environments, where medium or body fluids are periodically renewed. Samples were maintained at 37 °C in culture medium, which was either partially replaced or simply supplemented every 2–3 days. As shown in Fig. 4F, G, partial medium replacement reduced hydrogel stability: after 35 days, hydrogels lost ~30% of their initial weight, whereas simple cell medium addition resulted in only ~10% loss after 42 days. Based on these results, partial culture medium changes were used in subsequent cell culture experiments as they better represent physiological turnover [61].

Overall, our results demonstrate that the addition of HA, collagen, and BTO slightly increases stiffness and mechanical strength compared to Carr alone, while preserving injectability and favourable mechanical properties consistent with native soft tissues. Coupled with its simple preparation, without the need for precursor mixing [62,63], the proposed hydrogel represents an excellent candidate for regenerative applications *via* minimally invasive injection.

Given the goal of soft tissue regeneration, hydrogel porosity was also examined, as it strongly influences cell behaviour, migration, and differentiation. Hydrogels were freeze-dried, sectioned, and imaged internally using SEM. Collagen appeared to increase pore size relative to Carr, while the addition of BTO decreased pore size even compared to Carr alone, suggesting that although BTO does not affect mechanical properties or gelation, it modulates internal porosity (Fig. 5A).

The segmentation of SEM images provided quantitative insights into the pore morphology of carrageenan-based hydrogels with different compositional modifications. In Fig. 5A a single SEM image and the result of its segmentation for each sample and from each magnification is reported. The complete analysis was done using a larger set of images. The results of the segmentation are reported in Fig. 5B. In terms of aspect ratio (AR), the Carr sample displayed moderately elongated pores (mean AR = 2.30 ± 1.33), while the addition of collagen increased pore heterogeneity, with Carr_Coll exhibiting the highest standard deviation (AR StD = 3.94), suggesting less uniformity in pore shape. The incorporation of HA alone (Carr_HA) instead promoted more isotropic pores, as indicated by the lowest AR values (1.68 ± 0.65), consistent with the stiffening and homogenizing effect of HA on the polymeric network. Interestingly, the ternary Carr_Coll_HA hydrogel showed an increased AR (2.45 ± 0.78), indicating that the simultaneous presence of both collagen and HA restored a degree of elongation to the pore structure. A similar trend was observed in the Carr_Coll_HA_BTO formulation (2.27 ± 0.92), where the AR values suggest relatively elongated but consistent pore shapes. Pore symmetry (Sym) remained relatively stable across the different formulations, with values ranging from 0.776 to 0.806, indicating that despite compositional changes, the pores maintained a comparable degree of isotropy. The equivalent pore diameter (EqD) showed more substantial variations. The smallest pores were observed in Carr_HA (108.88 ± 129.59 μm), consistent with the densifying effect of HA, whereas Carr_Coll_HA showed the largest pores (465.24 ± 343.41 μm), suggesting a synergistic effect of collagen and hyaluronic acid in promoting larger pore formation. Carr_Coll_HA_BTO also exhibited large pores (365.85 ± 324.51 μm), though slightly smaller than those in the Carr_Coll_HA formulation. The pore area (A) followed similar trends, with Carr_HA showing the smallest values (22,439.9 ± 54,803.8 μm^2) and Carr_Coll_HA and Carr_Coll_HA_BTO reaching the highest mean areas (259,976.4 ± 406,766.4 μm^2 and 186,105.0 ± 484,590.6 μm^2, respectively).

Overall, the quantitative analysis indicates that all formulations exhibit an interconnected porous architecture with pore sizes and morphologies falling within a range considered suitable for hydrogel-based biomedical applications, supporting mass transport while preserving structural integrity.

3.2. *In vitro preliminary biological evaluation*

To preliminarily investigate the biological effects of the different formulations (Carr, Carr_HA, Carr_Coll, and Carr_HA_Coll), a human skin fibroblast cell line (WS1) was selected, as fibroblasts are key components of the ECM and WS1 cells are widely used as a standard model for initial biomaterial screening. This stepwise approach was designed to progressively evaluate formulations with increasing complexity, enabling a systematic assessment of the contribution of each component. Cells were encapsulated within the hydrogels, and their viability were assessed at two time points (day 1 and day 3). LIVE/DEAD assay showed a predominance of viable cells in all the formulations (Fig. 6A),

A

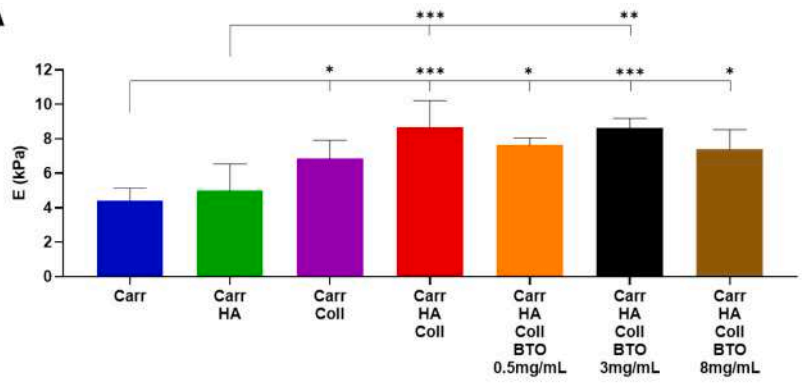

B

	E (kPa)
Carr	4.4 ± 0.7
Carr_HA_Coll	8.7 ± 1.5
Carr_HA	5.0 ± 1.5
Carr_Coll	6.9 ± 1.1
Carr_HA_Coll_BTO_0.5	7.6 ± 0.4
Carr_HA_Coll_BTO_3	8.6 ± 0.6
Carr_HA_Coll_BTO_8	7.4 ± 1.1

C

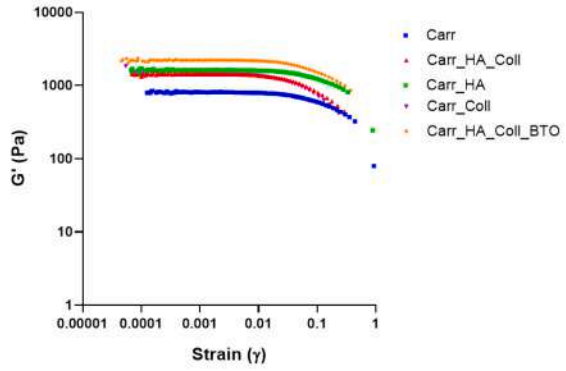

D

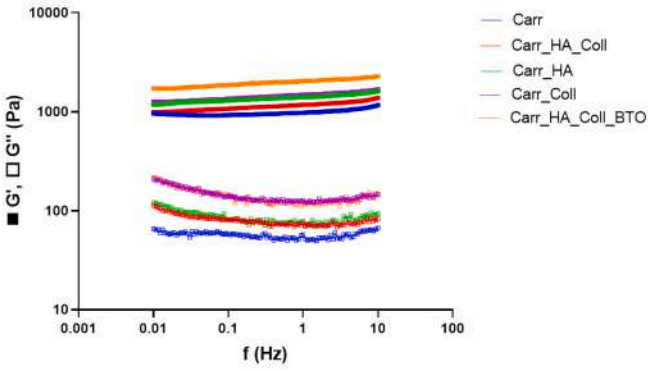

E

	Carr	Carr_HA_Coll	Carr_HA	Carr_Coll	Carr_HA_Coll_BTO
G'0 (kPa)	0.96 ± 0.10	1.47 ± 0.17	1.64 ± 0.07	1.62 ± 0.29	2.25 ± 0.51
G (kPa)	1.17 ± 0.13	2.11 ± 0.43	2.50 ± 0.61	2.88 ± 0.67	3.94 ± 1.12
γ* (%)	1.48 ± 1.07	1.18 ± 0.56	1.41 ± 0.54	0.60 ± 0.14	1.30 ± 0.70
tan δ	0.06 ± 0.01	0.07 ± 0.01	0.06 ± 0.01	0.10 ± 0.02	0.07 ± 0.02

F

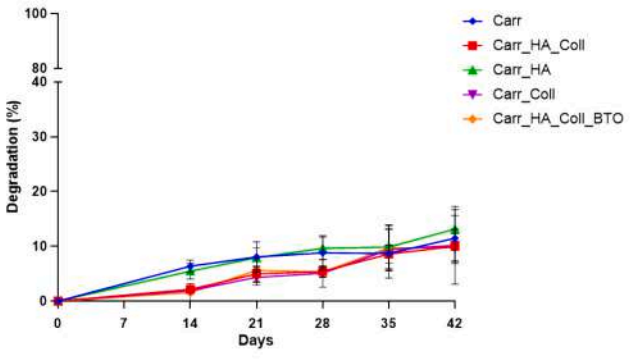

G

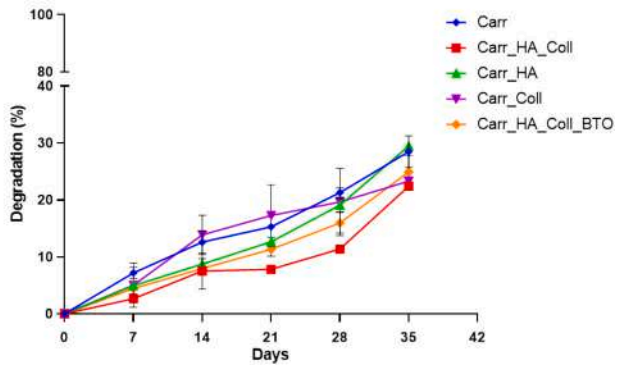

Fig. 4. A, B: Dynamic mechanical analysis (Young's Modulus); *p value ≤0.05, **p value ≤0.01, and ***p value ≤0.001. C-E: Rheological characterisation, (C) Stress sweep test (f = 1 Hz). (D) Frequency sweep test (stress = 5 Pa), (E) Viscoelastic properties evaluation. Storage modulus (G'0), Critical strain (γ*), shear modulus (G) and tan δ (G"/G). F. Hydrogel degradation profile over time with cell medium addition, expressed as % weight loss relative to day 0. G. Hydrogel degradation profile over time with partial medium replacement, expressed as % weight loss relative to day 0.

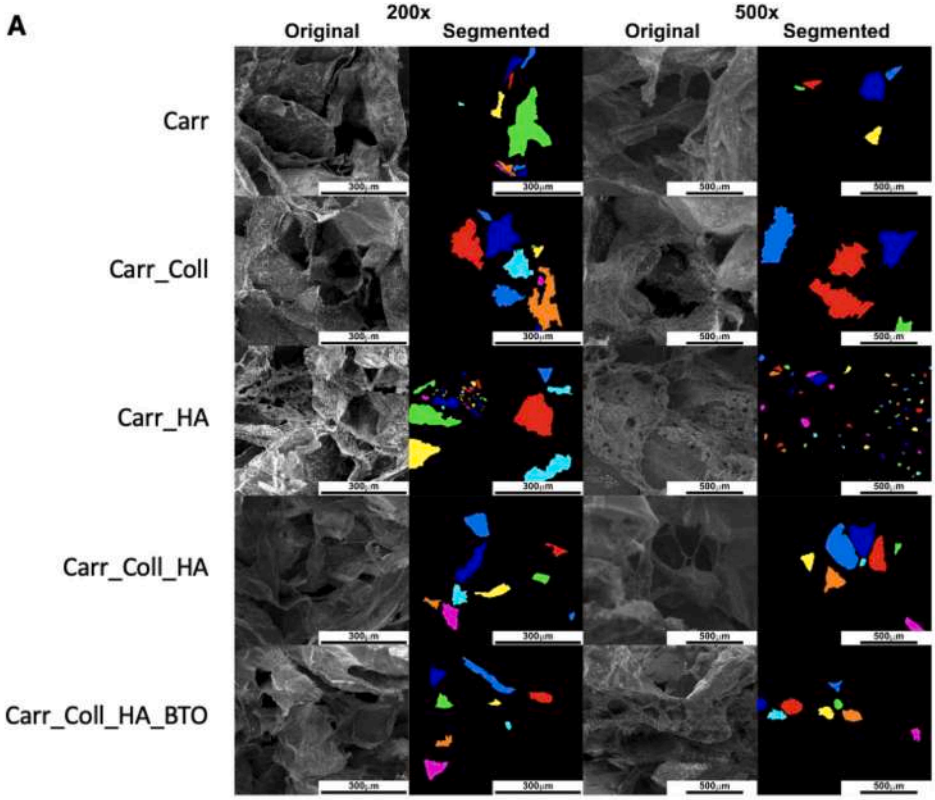

B

Sample	Mean AR	StD AR	Mean Sym	StD Sym	Mean EqD (μm)	StD EqD (μm)	Mean A (μm²)	StD A (μm²)
Carr	2.297	1.328	0.8	0.175	193.354	257.983	80610.3	186880.4
Carr_Coll	2.692	3.936	0.793	0.221	239.189	372.621	152253.2	390941.2
Carr_HA	1.683	0.648	0.806	0.100	108.879	129.593	22439.9	54803.8
Carr_HA_Coll	2.453	0.777	0.776	0.090	465.244	343.408	259976.4	406766.4
Carr_HA_Coll_BTO	2.273	0.921	0.799	0.088	365.848	324.507	186105.0	484590.6

Fig. 5. A: SEM micrographs and pore segmentation. A single explanatory image for each magnification (200× and 500×) and for each sample has been reported. The complete data analysis was conducted with a minimum of three images for each sample and for each magnification. B: Descriptive statistics of the distributions of the quantitative data obtained by segmentation. We quantified the aspect ratio (AR ≥ 1), the symmetry (0 ≤ Sym ≤ 1), the equivalent diameter (EqD) and the Area (A).

indicating that the hydrogel environment did not exert cytotoxic effects. Quantitative analysis using the PrestoBlue assay further confirmed that metabolic activity was maintained over time, with no statistically significant differences between day 1 and day 3 (Fig. 6B). Notably, cells displayed a predominantly rounded morphology within the hydrogel matrix, suggesting limited cell spreading under these conditions, which may reflect restricted cell–matrix interactions within the current formulation.

Based on these findings and given the overall cytocompatibility observed across all tested formulations, further biological characterisation was focused on Carr_HA_Coll, Carr alone, and a 2D control. Two additional cell lines relevant to soft tissue environments were selected: SH-SY5Y cells are widely used as an *in vitro* model for neuronal differentiation and regeneration, while C2C12 myoblasts are a well-established model for skeletal muscle differentiation and regeneration [64,65]. Cell viability and proliferation were evaluated at days 1 and 3 post-embedding. Consistent with previous observations, no differences between the two hydrogel formulations were detected for either cell line, and both showed increased viability by day 3, indicating cell proliferation and overall well-being (Fig. 6D, F). LIVE/DEAD staining again confirmed a predominance of viable cells (Fig. 6C, E).

To further elucidate the immunological profile of the hydrogels, an evaluation using murine macrophages (RAW 264.7) was conducted [62,66]. Macrophages play a central role in mediating adverse immune reactions to implanted materials, known as the foreign body response, an extensively documented phenomenon [62,67]. Upon contact with biomaterials, macrophages may polarise toward either a pro-inflammatory M1 phenotype or a pro-regenerative M2 phenotype, depending on microenvironmental cues [68]. RAW 264.7 cells were encapsulated in the hydrogels, and their viability after 48 h was confirmed by MTT assay and LIVE/DEAD staining (Fig. 6G, H).

Gene expression analysis of canonical M1/M2 markers (TNF-α for M1; IL-10 for M2) revealed a statistically significant upregulation of IL-10 in both Carr and Carr_HA_Coll compared to 2D controls (Fig. 6J). Moreover, Carr_HA_Coll exhibited the highest IL-10 expression, consistent with literature reporting HA-induced M2 activation and with recent

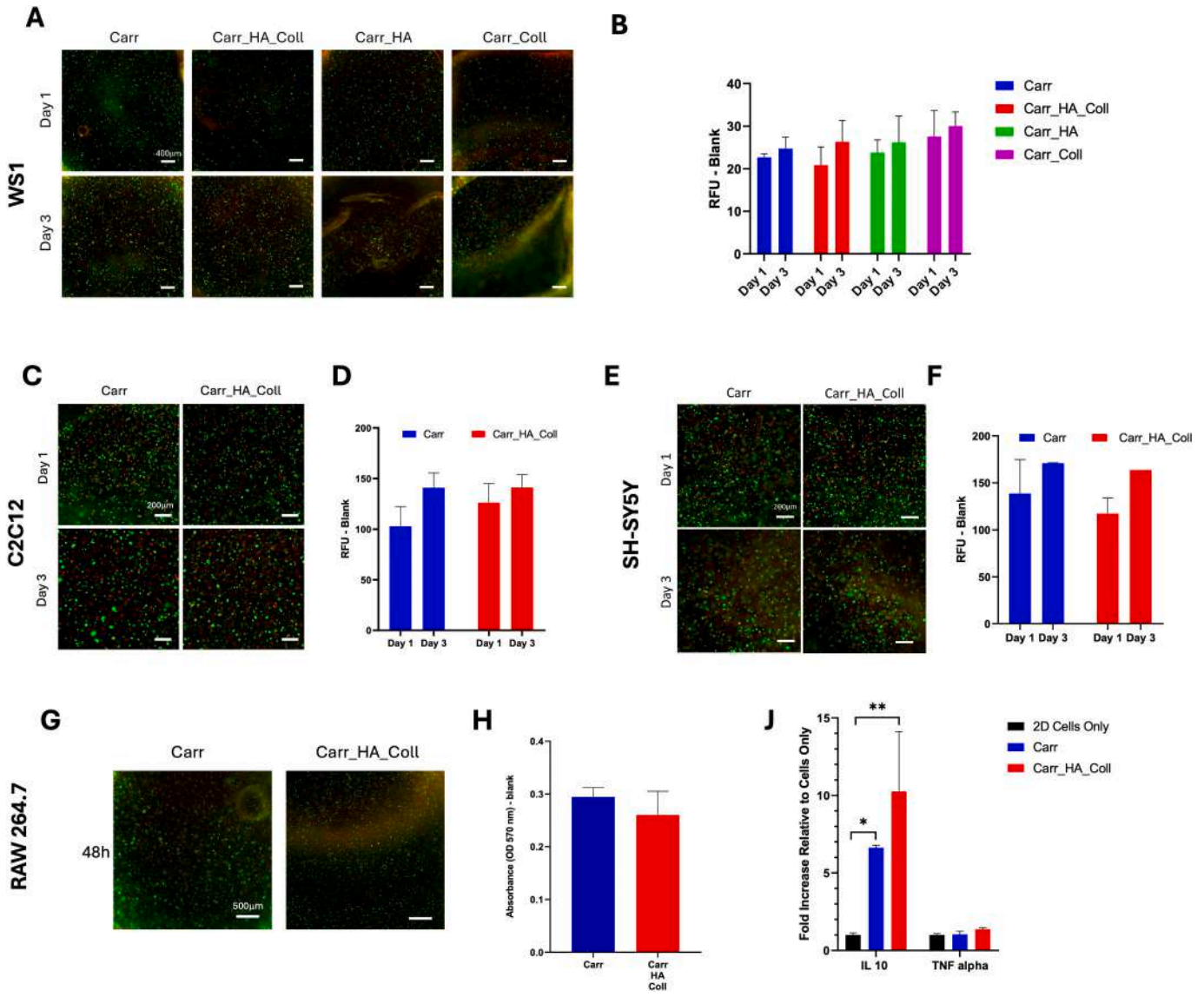

Fig. 6. LIVE/DEAD assay to assess viability of WS1 (A); C2C12 (C); SH-SY5Y (E) and RAW 264.7 (G) cells embedded in the hydrogels. Live cells in green; dead cells in red. B: WS1 cell proliferation measured by PrestoBlue test after 1 and 3 days of culture (mean ± SEM, $n = 3$). D: C2C12 Cell proliferation measured by PrestoBlue test after 1 and 3 days of culture (mean ± SEM, $n = 3$). F: SH-SY5Y Cell proliferation measured by PrestoBlue test after 1 and 3 days of culture (mean ± SEM, $n = 3$). H: F: RAW 264.7 Cell proliferation measured by MTT test after 2 days of culture (mean ± SEM, $n = 3$). J: Relative quantification IL-10 and TNF alpha gene expression after 2 days of culture. Data are presented as mean ± SEM relative to 2D cells only used as the control. *p value ≤0.05, **p value ≤0.01.

evidence showing that, although carrageenans are traditionally used as pro-inflammatory agents, κ-carrageenan and its oligosaccharides can also promote anti-inflammatory responses, including increased IL-10 secretion, depending on their molecular characteristics [69–71].

Collectively, these preliminary *in vitro* results demonstrate that the proposed injectable hydrogel provides a supportive microenvironment capable of sustaining the viability and proliferation of fibroblasts, neuronal-like cells, and muscle cells. Additionally, the material promotes macrophage polarisation toward a pro-regenerative phenotype, thereby contributing to a microenvironment conducive to tissue repair.

3.3. *Preliminary in vitro assessment of cell viability and proliferation under ultrasound-triggered piezoelectric stimulation*

Given the promising preliminary biological results and the growing evidence that bioelectric cues regulate skin physiology and wound healing [21], we conducted a preliminary assessment of the effect of BTO-mediated piezoelectric stimulation on cell viability following ultrasound (US) application. Although bioelectricity is traditionally associated with excitable tissues such as muscle and nerve, endogenous electric fields also play an important role in skin repair processes and in the regulation of dermal fibroblast behaviour. BTO is a piezoelectric material, and ultrasound induces mechanical deformation of BTO particles, generating local electric currents. To enable this piezoelectric effect, BTO particles were successfully polarised, as confirmed by nanoscale piezoresponse measurements, ensuring the presence of a stable piezoelectric behaviour necessary for effective electromechanical stimulation. Importantly, in the present system BTO particles are embedded as submicrometric fillers (~700 nm) within a crosslinked hydrogel network, which ensures strong physical confinement and limits particle mobility during stimulation, thereby maintaining the effect at a local, matrix-bound level. WS1 cells, chosen as a representative skin-derived fibroblast cell model, were encapsulated within Carr_HA_Coll_BTO, while Carr_HA_Coll without BTO served as the control. Hydrogels were either subjected to ultrasound stimulation or kept untreated. Specifically, WS1-laden hydrogels were exposed to daily

ultrasound stimulation for 60 s over five consecutive days at 900 mW/cm^2, a level reported in the literature to promote cellular activity [39,40]. Cell viability was evaluated both qualitatively, using LIVE/DEAD staining, and quantitatively, using the MTT assay. No significant differences were observed between the groups, neither due to the presence of BTO nor to ultrasound stimulation (Fig. 7). These results indicate that, under the applied conditions, piezoelectric stimulation does not affect cell viability. Accordingly, these findings should be interpreted as an initial confirmation of stimulation safety and system compatibility, rather than evidence of functional bioelectric effects. Future studies will explore whether adjusting ultrasound intensity, exposure duration, or investigating specific molecular pathways could reveal functional effects on WS1 cells, and other relevant cell types, including myoblasts, neuronal cells, and immune cells, to better assess tissue-specific and immunomodulatory responses. These directions are consistent with our previous findings using a different BTO-based system [72], where ultrasound-mediated piezoelectric stimulation did not affect cell viability or proliferation but modulated more complex cellular functions, including adhesion, Ca^{2+}-dependent signalling, and lineage-specific differentiation, as shown through dedicated mechanistic analyses.

3.4. Correlation analysis of hydrogel properties and cellular responses

To gain a deeper understanding of how hydrogel composition and structural properties relate to cellular responses across all tested cell lines, we performed a comprehensive correlation analysis. This approach allowed us to explore the interplay between mechanical, morphometric, and biological parameters, providing insights beyond the preliminary viability assessments. The results of the correlation matrix for composite hydrogels provide a view of how various quantitative parameters interact, as illustrated and quantified by the table and two complementary figures. The Spearman correlation matrix offers a comprehensive overview by quantifying the relationships among mechanical and morphometric variables, with the triangular heatmap in Fig. 8A visually communicating correlation strengths (coefficients above 0.4 or below −0.4 are considered moderate and those above 0.8 or below −0.8 are especially strong) while the upper triangle displays exact values for precise interpretation; simultaneously, Fig. 8B presents the corresponding *p*-values, clearly marking which correlations are statistically significant, with those below 0.05 flagged and those less than 0.001 shown as 0 for enhanced clarity. Robust associations ($r \geq 0.8$ and $p \leq 0.05$) are reported in Table 1.

The data reveal robust associations, such as the strong positive relationship between mean diameter and mean area, or between mean diameter and standard deviation of area, indicating that structural features affecting pore size are closely linked to properties like overall area and variability within the composite hydrogels; similar interconnections are observed between gel mechanics (Elastic modulus) and pore metrics (both area and diameter), reinforcing the notion that compositional adjustments impact both the microstructure and the resulting physical behaviour in measurable ways.

The correlation analysis also revealed strong and significant associations involving vitality at day 3, which are integral to understanding the interplay between cellular responses and hydrogel properties. Notably, the vitality at day 3 exhibited a perfect positive correlation with several parameters, such as tan δ and G*, with Spearman correlation coefficients of 1 and −1, respectively, and p-values reported as 0 (denoting very high statistical significance). Additionally, there were perfect negative correlations ($r = -1$, $p = 0$) with some other viability measures, indicating highly structured and distinct relationships across timepoints within the data set. When discussing these findings alongside the broader correlation matrix, it becomes clear that the vitality at day 3 is closely linked not only to mean measures of cell viability but also to the variability in those responses, as well as to multiple mechanical hydrogel properties captured in the matrix and detailed figures, reinforcing the pivotal role of third-day vitality as a sensitive and integrated indicator of the material's biological performance.

4. Conclusions

In this work, we developed an injectable carrageenan-based hydrogel designed as a versatile and biomimetic platform for regenerative applications. By combining κ/λ-carrageenan with key extracellular matrix components (*i.e.* HA and type I collagen), we obtained a multicomponent hydrogel that closely mimics the hydrated, compliant, and porous nature of native soft tissues. Ion-triggered gelation enabled rapid sol–gel transition under mild and physiologically relevant conditions, allowing straightforward delivery through fine-gauge needles and effective conformation to irregular defects.

The resulting hydrogels exhibited mechanical and viscoelastic properties comparable to those of soft tissues, like skeletal muscle and the central nervous system, together with a stable and interconnected porous architecture that supports mass transport and cell encapsulation. *In vitro* studies demonstrated cytocompatibility across multiple cell types relevant to soft tissue environments, including fibroblasts, myoblasts, neuronal cells, and macrophages. Notably, the hydrogel promoted a pro-regenerative macrophage response, suggesting a favourable immunomodulatory profile.

The incorporation of barium titanate particles endowed the system

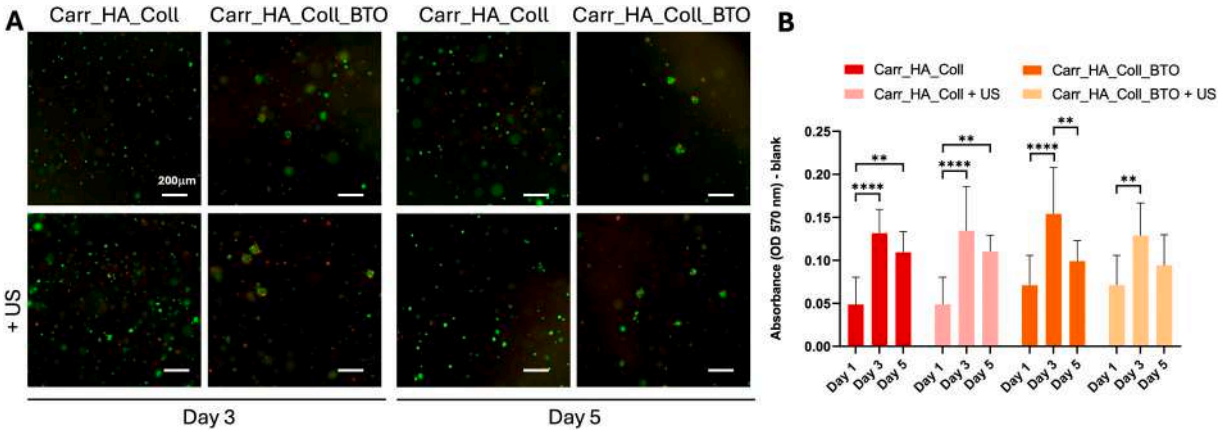

Fig. 7. A: LIVE/DEAD assay to assess the viability of WS1 cells embedded in the hydrogels after 3 and 5 days with or without US application. Live cells in green; dead cells in red ($n = 3$). B: Cell proliferation measured by MTT test after 1, 3 and 5 days of culture with or without US application. (mean ± SEM, $n = 9$). $^{**}p$ value ≤0.01, $^{****}p$ value ≤0.0001.

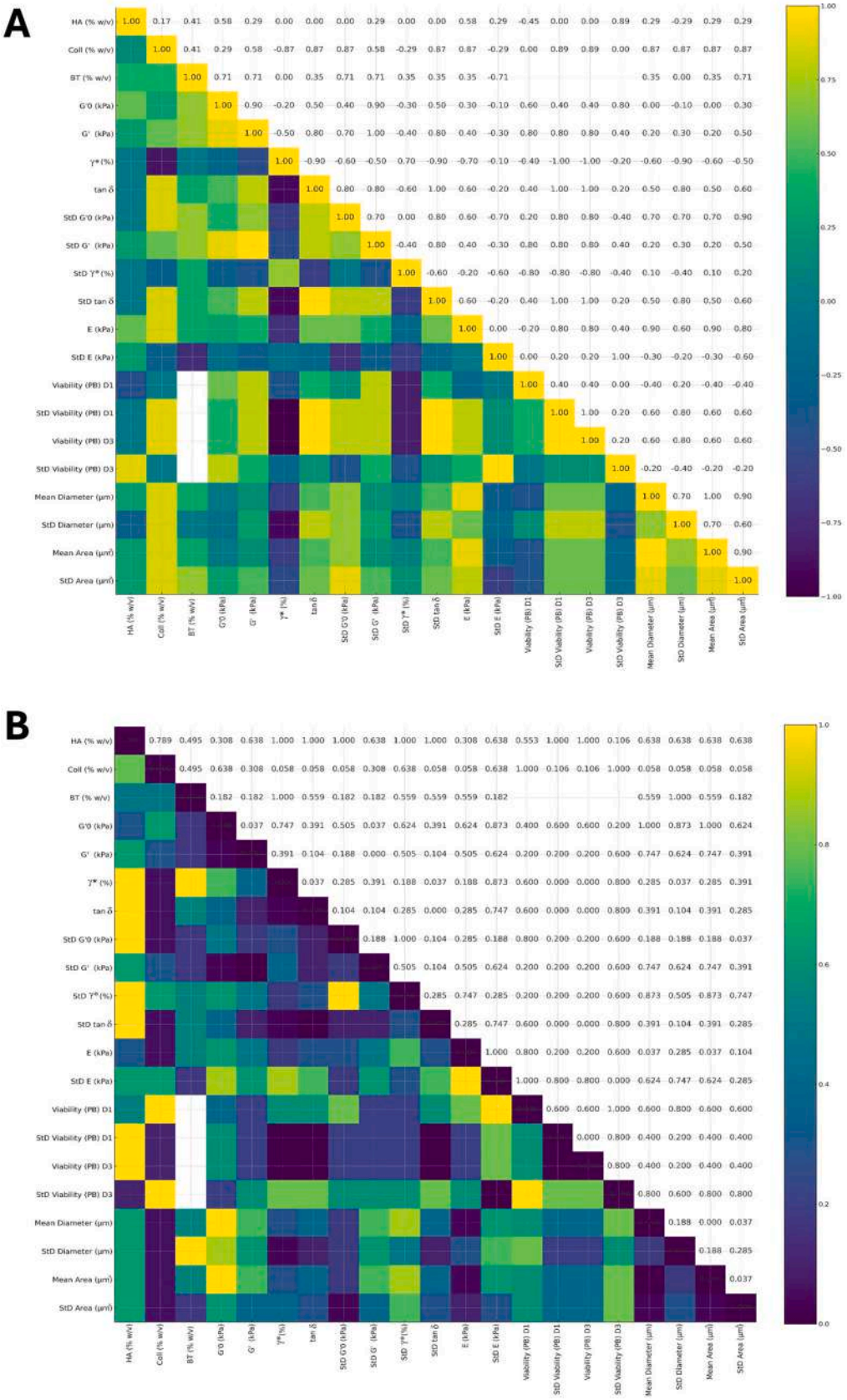

Fig. 8. A: Spearman's correlation matrix heatmap. The matrix shows the correlation coefficient r. A perfect correlation direct or inverse correlation is achieved when r is equal to +1 or −1, respectively. The correlation is considered moderate with a $\rho > 0.4$ or $\rho < -0.4$. B. *P*-values associated with the Spearman's correlation matrix. We considered statistically significant p-values $p \leq 0.05$. All values above 0.1 were considered not significant.

Table 1
Statistically significant ($p \leq 0.05$) strong ($r \geq 0.8$) correlations. It should be noticed that values of p lower than 0.001 have been reported as 0.

Variable 1	Variable 2	Corr	*p*-value	p
tan δ	Viability (PB) D3	1	0	0
G* (%)	Viability (PB) D3	1	0	0
E (kPa)	Mean Area (μm^2)	0.9	0.0374	0.0374
E (kPa)	Mean Diameter (μm^2)	0.9	0.0374	0.0374

with stimuli-responsive functionality without adversely affecting injectability, mechanical performance, or cell viability. Preliminary ultrasound stimulation experiments confirmed the safety of this approach, establishing a foundation for future investigations aimed at elucidating functional bioelectric effects and tissue-specific regenerative outcomes.

It should be noted that this study is limited to *in vitro* validation and proof-of-concept demonstration. Therefore, translational performance, long-term biocompatibility, and degradation behaviour under physiological conditions remain to be established in future preclinical *in vivo* studies. Future developments may also benefit from optimisation strategies reported in the literature, including surface functionalisation or coating of BTO particles and the exploration of combination with other piezoelectric materials, which could improve particle dispersion within the hydrogel matrix and enable more controlled cell–material interactions, including the possibility of cell-targeting approaches and modulation of specific cellular pathways.

Overall, the proposed hydrogel represents a simple, user-friendly, and cost-effective injectable system with potential for minimally invasive regenerative therapies. Its modular design and responsiveness to external stimuli make it a promising platform for further optimisation and application in soft tissue regeneration.

CRediT authorship contribution statement

Arianna Rossi: Writing – review & editing, Writing – original draft, Methodology, Investigation, Formal analysis. **Noemi Ravaglia:** Investigation. **Federica Arienti:** Methodology. **Pietro Galizia:** Formal analysis, Writing – review & editing. **Massimiliano Labardi:** Investigation, Formal analysis, Writing – review & editing. **Carlo Baldisserri:** Investigation. **Rosa Mancinelli:** Writing – review & editing. **Sabrina Angelini:** Writing – review & editing. **Monica Montesi:** Writing – review & editing, Writing – original draft. **Alessio Bucciarelli:** Writing – original draft, Investigation, Formal analysis. **Elisa Mercadelli:** Writing – review & editing, Formal analysis. **Silvia Panseri:** Writing – review & editing, Writing – original draft, Supervision, Funding acquisition, Conceptualization.

Declaration of Generative AI and AI-assisted technologies in the writing process

During the preparation of this work, the authors used ChatGPT (OpenAI) for final English language editing and improvement of text clarity. After using this tool, the authors carefully reviewed and edited the content as needed and take full responsibility for the content of the published article.

Declaration of competing interest

The authors declare that they have no known competing financial interests or personal relationships that could have appeared to influence the work reported in this paper.

Acknowledgements

This work was supported by MUR: Missione 4 Componente 2, Investimento 3.3 dottorati innovativi (DM 630), Università degli Studi G. d'Annunzio Chieti – Pescara, CUP D53C24002620003 (40-033-53-DOT1353500-15075) and Alma Mater Studiorum – Università di Bologna, CUP J33C24001540009 (40-033-03-DOT1303545-11841). Margherita Montorsi (CNR-IPCF) is acknowledged for assistance with BTO nanoparticle sample preparation for PFM study, and for useful discussion.

Appendix A. Supplementary data

Supplementary data to this article can be found online at https://doi.org/10.1016/j.ijbiomac.2026.153953.

Data availability

Data will be made available on request.

References

[1] A. Bois, C. Grandela, J. Gallant, C. Mummery, P. Menasché, Revitalizing the heart: strategies and tools for cardiomyocyte regeneration post-myocardial infarction, npj Regener. Med. 10 (1) (2025) 6, https://doi.org/10.1038/s41536-025-00394-2.
[2] A. Kengelbach-Weigand, C. Thielen, T. Bäuerle, R. Götzl, T. Gerber, C. Körner, J. P. Beier, R.E. Horch, A.M. Boos, Personalized medicine for reconstruction of critical-size bone defects – a translational approach with customizable vascularized bone tissue, npj Regener. Med. 6 (1) (2021) 49, https://doi.org/10.1038/s41536-021-00158-8.
[3] H. Kwon, W.E. Brown, C.A. Lee, D. Wang, N. Paschos, J.C. Hu, K.A. Athanasiou, Surgical and tissue engineering strategies for articular cartilage and meniscus repair, Nat. Rev. Rheumatol. 15 (9) (2019) 550–570, https://doi.org/10.1038/s41584-019-0255-1.
[4] E.A. Lucich, J.L. Rendon, I.L. Valerio, Advances in addressing full-thickness skin defects: a review of dermal and epidermal substitutes, Regen. Med. 13 (4) (2018) 443–456, https://doi.org/10.2217/rme-2017-0047.
[5] M. Moradi, B. Hood, M. Moradi, A. Atala, The potential role of regenerative medicine in the management of traumatic patients, J. Injury Violence Res. (2014), https://doi.org/10.5249/jivr.v7i1.704.
[6] T. Nuge, Z. Liu, X. Liu, B.C. Ang, A. Andriyana, H.S.C. Metselaar, M.E. Hoque, Recent advances in scaffolding from natural-based polymers for volumetric muscle injury, Molecules 26 (3) (2021) 699, https://doi.org/10.3390/molecules26030699.
[7] M. Quarta, M. Cromie, R. Chacon, J. Blonigan, V. Garcia, I. Akimenko, M. Hamer, P. Paine, M. Stok, J.B. Shrager, T.A. Rando, Bioengineered constructs combined with exercise enhance stem cell-mediated treatment of volumetric muscle loss, Nat. Commun. 8 (1) (2017) 15613, https://doi.org/10.1038/ncomms15613.
[8] S. Norouzi, N. Saveh Shemshaki, E. Norouzi, M. Latifi, B. Azimi, S. Danti, X. Qiao, Y. Miao, S. Yang, M. Gorji, V. Petrovic, M.A. Aboudzadeh, R. Bagherzadeh, Recent advances in biomaterials for tissue-engineered constructs: essential factors and engineering techniques, Mater. Today Chem. 37 (2024) 102016, https://doi.org/10.1016/j.mtchem.2024.102016.
[9] A.K. Gaharwar, I. Singh, A. Khademhosseini, Engineered biomaterials for in situ tissue regeneration, Nat. Rev. Mater. 5 (9) (2020) 686–705, https://doi.org/10.1038/s41578-020-0209-x.
[10] M. Rahmati, D.K. Mills, A.M. Urbanska, M.R. Saeb, J.R. Venugopal, S. Ramakrishna, M. Mozafari, Electrospinning for tissue engineering applications, Prog. Mater. Sci. 117 (2021) 100721, https://doi.org/10.1016/j.pmatsci.2020.100721.
[11] A. Senthamizhan, B. Balusamy, T. Uyar, Electrospinning, in: Electrospun Materials for Tissue Engineering and Biomedical Applications, Elsevier, 2017, pp. 3–41, https://doi.org/10.1016/B978-0-08-101022-8.00001-6.
[12] L. Moroni, J.A. Burdick, C. Highley, S.J. Lee, Y. Morimoto, S. Takeuchi, J.J. Yoo, Biofabrication strategies for 3D in vitro models and regenerative medicine, Nat. Rev. Mater. 3 (5) (2018) 21–37, https://doi.org/10.1038/s41578-018-0006-y.
[13] C. Mota, S. Camarero-Espinosa, M.B. Baker, P. Wieringa, L. Moroni, Bioprinting: from tissue and organ development to *in vitro* models, Chem. Rev. 120 (19) (2020) 10547–10607, https://doi.org/10.1021/acs.chemrev.9b00789.
[14] J.P.M. Sousa, E. Stratakis, J. Mano, P.A.A.P. Marques, Anisotropic 3D scaffolds for spinal cord guided repair: current concepts, Biomater. Adv. 148 (2023) 213353, https://doi.org/10.1016/j.bioadv.2023.213353.
[15] F. Wahid, T. Khan, Z. Hussain, H. Ullah, Nanocomposite scaffolds for tissue engineering; properties, preparation and applications, in: Applications of Nanocomposite Materials in Drug Delivery, Elsevier, 2018, pp. 701–735, https://doi.org/10.1016/B978-0-12-813741-3.00031-5.
[16] S. Jana, S.K.L. Levengood, M. Zhang, Anisotropic materials for skeletal-muscle-tissue engineering, Adv. Mater. 28 (48) (2016) 10588–10612, https://doi.org/10.1002/adma.201600240.
[17] Md.T.I. Mredha, I. Jeon, Biomimetic anisotropic hydrogels: advanced fabrication strategies, extraordinary functionalities, and broad applications, Prog. Mater. Sci. 124 (2022) 100870, https://doi.org/10.1016/j.pmatsci.2021.100870.
[18] A.P. Mathew, S. Uthaman, K.-H. Cho, C.-S. Cho, I.-K. Park, Injectable hydrogels for delivering biotherapeutic molecules, Int. J. Biol. Macromol. 110 (2018) 17–29, https://doi.org/10.1016/j.ijbiomac.2017.11.113.

[19] A. Mellati, E. Hasanzadeh, M. Gholipourmalekabadi, S.E. Enderami, Injectable nanocomposite hydrogels as an emerging platform for biomedical applications: a review, Mater. Sci. Eng. C 131 (2021) 112489, https://doi.org/10.1016/j.msec.2021.112489.
[20] S. Yue, H. He, B. Li, T. Hou, Hydrogel as a biomaterial for bone tissue engineering: a review, Nanomaterials 10 (8) (2020) 1511, https://doi.org/10.3390/nano10081511.
[21] S. Zhao, A.S. Mehta, M. Zhao, Biomedical applications of electrical stimulation, Cell. Mol. Life Sci. 77 (14) (2020) 2681–2699, https://doi.org/10.1007/s00018-019-03446-1.
[22] H.-S. Kim, T. Baby, J.-H. Lee, U.S. Shin, H.-W. Kim, Biomaterials-enabled electrical stimulation for tissue healing and regeneration, Med-X 2 (1) (2024) 7, https://doi.org/10.1007/s44258-024-00020-8.
[23] A. De Pieri, S. Rana, S. Korntner, D.I. Zeugolis, Seaweed polysaccharides as macromolecular crowding agents, Int. J. Biol. Macromol. 164 (2020) 434–446, https://doi.org/10.1016/j.ijbiomac.2020.07.087.
[24] M. Raghunath, D.I. Zeugolis, Transforming eukaryotic cell culture with macromolecular crowding, Trends Biochem. Sci. 46 (10) (2021) 805–811, https://doi.org/10.1016/j.tibs.2021.04.006.
[25] R. Tuvikene, Carrageenans, in: Handbook of Hydrocolloids, Elsevier, 2021, pp. 767–804, https://doi.org/10.1016/B978-0-12-820104-6.00006-1.
[26] M. Younes, P. Aggett, F. Aguilar, R. Crebelli, M. Filipič, M.J. Frutos, P. Galtier, D. Gott, U. Gundert-Remy, G.G. Kuhnle, C. Lambré, J. Leblanc, I.T. Lillegaard, P. Moldeus, A. Mortensen, A. Oskarsson, I. Stankovic, I. Waalkens-Berendsen, R. A. Woutersen, B. Dusemund, Re-evaluation of carrageenan (E 407) and processed *Eucheuma* seaweed (E 407a) as food additives, EFSA J. 16 (4) (2018), https://doi.org/10.2903/j.efsa.2018.5238.
[27] U.S. Food and Drug Administration, Substances Added to Food (formerly EAFUS): CARRAGEENAN. https://hfpappexternal.fda.gov/scripts/fdcc/index.cfm?set=FoodSubstances&id=CARRAGEENAN, 2025.
[28] C. Frantz, K.M. Stewart, V.M. Weaver, The extracellular matrix at a glance, J. Cell Sci. 123 (24) (2010) 4195–4200, https://doi.org/10.1242/jcs.023820.
[29] N.K. Karamanos, A.D. Theocharis, Z. Piperigkou, D. Manou, A. Passi, S. S. Skandalis, D.H. Vynios, V. Orian-Rousseau, S. Ricard-Blum, C.E.H. Schmelzer, L. Duca, M. Durbeej, N.A. Afratis, L. Troeberg, M. Franchi, V. Masola, M. Onisto, A guide to the composition and functions of the extracellular matrix, FEBS J. 288 (24) (2021) 6850–6912, https://doi.org/10.1111/febs.15776.
[30] S. Calve, J. Isaac, J.P. Gumucio, C.L. Mendias, Hyaluronic acid, HAS1, and HAS2 are significantly upregulated during muscle hypertrophy, Am. J. Physiol. Cell Physiol. 303 (5) (2012) C577–C588, https://doi.org/10.1152/ajpcell.00057.2012.
[31] S. Calve, S.J. Odelberg, H.-G. Simon, A transitional extracellular matrix instructs cell behavior during muscle regeneration, Dev. Biol. 344 (1) (2010) 259–271, https://doi.org/10.1016/j.ydbio.2010.05.007.
[32] N. Petit, Y.J. Chang, F.A. Lobianco, T. Hodgkinson, S. Browne, Hyaluronic acid as a versatile building block for the development of biofunctional hydrogels: in vitro models and preclinical innovations, Mater. Today Bio 31 (2025) 101596, https://doi.org/10.1016/j.mtbio.2025.101596.
[33] V. Buscaglia, M.T. Buscaglia, G. Canu, BaTiO3-based ceramics: fundamentals, properties and applications, in: Encyclopedia of Materials: Technical Ceramics and Glasses, Elsevier, 2021, pp. 311–344, https://doi.org/10.1016/B978-0-12-803581-8.12132-0.
[34] B. Jiang, J. Iocozzia, L. Zhao, H. Zhang, Y.-W. Harn, Y. Chen, Z. Lin, Barium titanate at the nanoscale: controlled synthesis and dielectric and ferroelectric properties, Chem. Soc. Rev. 48 (4) (2019) 1194–1228, https://doi.org/10.1039/C8CS00583D.
[35] B. Fan, Z. Guo, X. Li, S. Li, P. Gao, X. Xiao, J. Wu, C. Shen, Y. Jiao, W. Hou, Electroactive barium titanate coated titanium scaffold improves osteogenesis and osseointegration with low-intensity pulsed ultrasound for large segmental bone defects, Bioact. Mater. 5 (4) (2020) 1087–1101, https://doi.org/10.1016/j.bioactmat.2020.07.001.
[36] F. Furlani, M. Montanari, N. Sangiorgi, E. Saracino, E. Campodoni, A. Sanson, V. Benfenati, A. Tampieri, S. Panseri, M. Sandri, Electroconductive and injectable hydrogels based on gelatin and PEDOT:PSS for a minimally invasive approach in nervous tissue regeneration, Biomater. Sci. 10 (8) (2022) 2040–2053, https://doi.org/10.1039/D2BM00116K.
[37] M. Labardi, A. Magnani, S. Capaccioli, Piezoelectric displacement mapping of compliant surfaces by constant-excitation frequency-modulation piezoresponse force microscopy, Nanotechnology 31 (7) (2020) 075707, https://doi.org/10.1088/1361-6528/ab52ca.
[38] K.J. Livak, T.D. Schmittgen, Analysis of relative gene expression data using real-time quantitative PCR and the 2−ΔΔCT method, Methods 25 (4) (2001) 402–408, https://doi.org/10.1006/meth.2001.1262.
[39] A. Cafarelli, A. Verbeni, A. Poliziani, P. Dario, A. Menciassi, L. Ricotti, Tuning acoustic and mechanical properties of materials for ultrasound phantoms and smart substrates for cell cultures, Acta Biomater. 49 (2017) 368–378, https://doi.org/10.1016/j.actbio.2016.11.049.
[40] M. Montorsi, C. Pucci, D. De Pasquale, A. Marino, M.C. Ceccarelli, M. Mazzuferi, M. Bartolucci, A. Petretto, M. Prato, D. Debellis, G. De Simoni, G. Pugliese, M. Labardi, G. Ciofani, Ultrasound-activated piezoelectric nanoparticles trigger microglia activity against glioblastoma cells, Adv. Healthc. Mater. 13 (18) (2024), https://doi.org/10.1002/adhm.202304331.
[41] A. Djalali-Cuevas, M. Rettel, F. Stein, M. Savitski, S. Kearns, J. Kelly, M. Biggs, I. Skoufos, A. Tzora, N. Prassinos, N. Diakakis, D.I. Zeugolis, Macromolecular crowding in human tenocyte and skin fibroblast cultures: a comparative analysis, Mater. Today Bio 25 (2024) 100977, https://doi.org/10.1016/j.mtbio.2024.100977.
[42] S. Du, S.J. Elliman, D.I. Zeugolis, T. O'Brien, Carrageenan as a macromolecular crowding agent in human umbilical cord derived mesenchymal stromal cell culture, Int. J. Biol. Macromol. 251 (2023) 126353, https://doi.org/10.1016/j.ijbiomac.2023.126353.
[43] S.W. Fok, R.C.H. Gresham, W. Ryan, B. Osipov, C. Bahney, J.K. Leach, Macromolecular crowding and decellularization method increase the growth factor binding potential of cell-secreted extracellular matrices, Front. Bioeng. Biotechnol. 11 (2023), https://doi.org/10.3389/fbioe.2023.1091157.
[44] S. Garantziotis, R.C. Savani, Hyaluronan biology: a complex balancing act of structure, function, location and context, Matrix Biol. 78–79 (2019) 1–10, https://doi.org/10.1016/j.matbio.2019.02.002.
[45] T.J. McKee, G. Perlman, M. Morris, S.V. Komarova, Extracellular matrix composition of connective tissues: a systematic review and meta-analysis, Sci. Rep. 9 (1) (2019) 10542, https://doi.org/10.1038/s41598-019-46896-0.
[46] A. Omidinia-Anarkoli, S. Boesveld, U. Tuvshindorj, J.C. Rose, T. Haraszti, L. De Laporte, An injectable hybrid hydrogel with oriented short fibers induces unidirectional growth of functional nerve cells, Small 13 (36) (2017), https://doi.org/10.1002/smll.201702207.
[47] L. Wang, T. Li, Z. Wang, J. Hou, S. Liu, Q. Yang, L. Yu, W. Guo, Y. Wang, B. Guo, W. Huang, Y. Wu, Injectable remote magnetic nanofiber/hydrogel multiscale scaffold for functional anisotropic skeletal muscle regeneration, Biomaterials 285 (2022) 121537, https://doi.org/10.1016/j.biomaterials.2022.121537.
[48] C.-J. Cheng, E. Kuo, C.-L. Huang, Extracellular potassium homeostasis: insights from hypokalemic periodic paralysis, Semin. Nephrol. 33 (3) (2013) 237–247, https://doi.org/10.1016/j.semnephrol.2013.04.004.
[49] W. Chu, M. Nie, X. Ke, J. Luo, J. Li, Recent advances in injectable dual crosslinking hydrogels for biomedical applications, Macromol. Biosci. 21 (7) (2021), https://doi.org/10.1002/mabi.202100109.
[50] K. Peng, L. Zheng, T. Zhou, C. Zhang, H. Li, Light manipulation for fabrication of hydrogels and their biological applications, Acta Biomater. 137 (2022) 20–43, https://doi.org/10.1016/j.actbio.2021.10.003.
[51] A. Rossi, G. Bassi, C. Cunha, C. Baldisserri, N. Ravaglia, D. Gardini, F. Molinari, F. Lista, F.J. Teran, A. Piperno, M. Montesi, S. Panseri, Magnetically induced anisotropic structure in an injectable hydrogel for skeletal muscle regeneration, J. Colloid Interface Sci. 678 (2025) 334–345, https://doi.org/10.1016/j.jcis.2024.09.121.
[52] A. Rossi, F. Furlani, G. Bassi, C. Cunha, A. Lunghi, F. Molinari, F.J. Teran, F. Lista, M. Bianchi, A. Piperno, M. Montesi, S. Panseri, Contactless magnetically responsive injectable hydrogel for aligned tissue regeneration, Mater. Today Bio 27 (2024) 101110, https://doi.org/10.1016/j.mtbio.2024.101110.
[53] X. Tang, F. Zhou, S. Wang, G. Wang, L. Bai, J. Su, Bioinspired injectable hydrogels for bone regeneration, J. Adv. Res. 75 (2025) 163–188, https://doi.org/10.1016/j.jare.2024.10.032.
[54] M. Ćurčić, B. Hadžić, M. Gilić, Z. Lazarević, A. Ilić, BaTiO3 nanocarriers: advancing targeted therapies with smart drug release, Pharmaceutics 17 (9) (2025) 1203, https://doi.org/10.3390/pharmaceutics17091203.
[55] L. Roldan, C. Montoya, V. Solanki, K.Q. Cai, M. Yang, S. Correa, S. Orrego, A novel injectable piezoelectric hydrogel for periodontal disease treatment, ACS Appl. Mater. Interfaces 15 (37) (2023) 43441–43454, https://doi.org/10.1021/acsami.3c08336.
[56] P.M. Hinderliter, K.R. Minard, G. Orr, W.B. Chrisler, B.D. Thrall, J.G. Pounds, J. G. Teeguarden, ISDD: a computational model of particle sedimentation, diffusion and target cell dosimetry for in vitro toxicity studies, Part. Fibre Toxicol. 7 (1) (2010) 36, https://doi.org/10.1186/1743-8977-7-36.
[57] J.G. Teeguarden, P.M. Hinderliter, G. Orr, B.D. Thrall, J.G. Pounds, Particokinetics in vitro: dosimetry considerations for in vitro nanoparticle toxicity assessments, Toxicol. Sci. 95 (2) (2007) 300–312, https://doi.org/10.1093/toxsci/kfl165.
[58] K. Wittmaack, Novel dose metric for apparent cytotoxicity effects generated by in vitro cell exposure to silica nanoparticles, Chem. Res. Toxicol. 24 (2) (2011) 150–158, https://doi.org/10.1021/tx100331w.
[59] C.F. Guimarães, L. Gasperini, A.P. Marques, R.L. Reis, The stiffness of living tissues and its implications for tissue engineering, Nat. Rev. Mater. 5 (5) (2020) 351–370, https://doi.org/10.1038/s41578-019-0169-1.
[60] W.J. Tyler, The mechanobiology of brain function, Nat. Rev. Neurosci. 13 (12) (2012) 867–878, https://doi.org/10.1038/nrn3383.
[61] S.R. Caliari, J.A. Burdick, A practical guide to hydrogels for cell culture, Nat. Methods 13 (5) (2016) 405–414, https://doi.org/10.1038/nmeth.3839.
[62] L. García-Fernández, M. Olmeda-Lozano, L. Benito-Garzón, A. Pérez-Caballer, J. San Román, B. Vázquez-Lasa, Injectable hydrogel-based drug delivery system for cartilage regeneration, Mater. Sci. Eng. C 110 (2020) 110702, https://doi.org/10.1016/j.msec.2020.110702.
[63] Y. Zhao, Z. Cui, B. Liu, J. Xiang, D. Qiu, Y. Tian, X. Qu, Z. Yang, An injectable strong hydrogel for bone reconstruction, Adv. Healthc. Mater. 8 (17) (2019), https://doi.org/10.1002/adhm.201900709.
[64] S. Burattini, P. Ferri, M. Battistelli, R. Curci, F. Luchetti, E. Falcieri, C2C12 murine myoblasts as a model of skeletal muscle development: morpho-functional characterization, Eur. J. Histochem. 48 (3) (2004) 223–233.
[65] I.L. Targett, L.A. Crompton, M.E. Conway, T.J. Craig, Differentiation of SH-SY5Y neuroblastoma cells using retinoic acid and BDNF: a model for neuronal and synaptic differentiation in neurodegeneration, In Vitro Cell. Dev. Biol. - Anim. 60 (9) (2024) 1058–1067, https://doi.org/10.1007/s11626-024-00948-6.
[66] L.S. Saleh, S.J. Bryant, In vitro and in vivo models for assessing the host response to biomaterials, in: Drug Discovery Today: Disease Models Vol. 24, Elsevier Ltd, 2017, pp. 13–21, https://doi.org/10.1016/j.ddmod.2018.04.002.
[67] L. Kämmerling, L.E. Fisher, E. Antmen, G.M. Simsek, H.M. Rostam, N.E. Vrana, A. M. Ghaemmaghami, Mitigating the foreign body response through 'immune-

instructive' biomaterials, J. Immunol. Regen. Med. 12 (2021) 100040, https://doi.org/10.1016/j.regen.2021.100040.
[68] J.M. Anderson, A. Rodriguez, D.T. Chang, Foreign body reaction to biomaterials, Semin. Immunol. 20 (2) (2008) 86–100, https://doi.org/10.1016/j.smim.2007.11.004.
[69] S. Bhattacharyya, H. Liu, Z. Zhang, M. Jam, P.K. Dudeja, G. Michel, R.J. Linhardt, J.K. Tobacman, Carrageenan-induced innate immune response is modified by enzymes that hydrolyze distinct galactosidic bonds, J. Nutr. Biochem. 21 (10) (2010) 906–913, https://doi.org/10.1016/j.jnutbio.2009.07.002.
[70] B.M. Lee, S.J. Park, I. Noh, C.-H. Kim, The effects of the molecular weights of hyaluronic acid on the immune responses, Biomater. Res. 25 (1) (2021), https://doi.org/10.1186/s40824-021-00228-4.
[71] R. Song, X. Mao, S. Tang, κ/β-Carrageenan oligosaccharides promoting polarization of LPS-activated macrophage and their potential in diabetes wound healing, Mater. Sci. Eng. C 121 (2021) 111830, https://doi.org/10.1016/j.msec.2020.111830.
[72] N. Ravaglia, A. Rossi, M. Vignolo, P. Galizia, D. Pacheco, F. Arienti, C. Baldisserri, C.M. Guzzo, M. Montesi, R. Mancinelli, M. Labardi, T.M.F. Patrício, J. Glaum, C. Cunha, E. Mercadelli, G. Luciano, S. Panseri, 4D piezoceramic-integrated scaffolds with bioelectric cues for skeletal muscle regeneration, Bioact. Mater. 65 (2026) 1005–1018, https://doi.org/10.1016/j.bioactmat.2026.06.027.